

Strong magnon-magnon coupling and low dissipation rate in an all-magnetic-insulator heterostructure

Jiacheng Liu^{1,2,†}, Yuzan Xiong,^{3,‡} Jingming Liang,^{4,‡} Xuezhao Wu,^{1,2} Chen Liu,⁵ Shun Kong Cheung,^{1,2} Zheyu Ren^{1,2}, Ruizi Liu,^{1,2} Andrew Christy³, Zehan Chen^{1,2,6}, Yifan Liu,¹ Ferris Prima Nugraha^{1,2}, Xi-Xiang Zhang⁵, Dennis Chi Wah Leung,⁴ Wei Zhang,^{3,*} and Qiming Shao^{1,2,6,†}

¹Department of Electronic and Computer Engineering, The Hong Kong University of Science and Technology, Hong Kong SAR, China

²IAS Center for Quantum Technologies, The Hong Kong University of Science and Technology, Hong Kong SAR, China

³Department of Physics and Astronomy, The University of North Carolina at Chapel Hill, Chapel Hill, North Carolina 27599, USA

⁴Department of Applied Physics, The Hong Kong Polytechnic University, Hong Kong SAR, China

⁵Physical Science and Engineering Division (PSE), King Abdullah University of Science and Technology (KAUST), Thuwal 23955–6900, Saudi Arabia

⁶Department of Physics, The Hong Kong University of Science and Technology, Hong Kong SAR, China

(Received 7 November 2023; revised 23 May 2024; accepted 26 July 2024; published 9 September 2024)

Magnetic insulators, such as yttrium iron garnets (YIGs), are important for spin-wave or magnonic devices as their low damping enables low-power dissipation. Magnetic insulator heterostructures can offer larger design space for realizing exotic magnonic quantum states, provided that individual layers have low damping and their exchange coupling is strong and engineerable. Here, we show that, in a high-quality all-insulator thulium iron garnet (TmIG)/YIG bilayer system, TmIG exhibits an ultralow dissipation rate thanks to its low-damping, low-saturation magnetization and strong orbital momentum. The low dissipation rates in both YIG and TmIG, along with their significant coupling strength due to interfacial exchange coupling, enable strong and coherent magnon-magnon coupling. The coupling strength can be tuned by varying the magnetic insulator layer thickness and magnon modes, which is consistent with analytical calculations and micromagnetic simulations. Our results demonstrate TmIG/YIG as a novel platform for investigating hybrid magnonic phenomena and open opportunities for magnon devices comprising all-insulator heterostructures.

DOI: 10.1103/PhysRevApplied.22.034017

I. INTRODUCTION

Spin-wave (or magnonic) devices utilize the magnon spin degree of freedom to process information, which can occur in magnetic insulators free from any charge current and, therefore, are promising contenders for low-power functional circuits [1–5]. Magnetic garnets such as yttrium iron garnet ($\text{Y}_3\text{Fe}_5\text{O}_{12}$, YIG) possess a low-damping factor, which enables long magnon spin transmission [6,7], efficient magnon spin current generation [8], and magnon logic circuits [2,4]. Another type of magnetic garnet, i.e., thulium iron garnet ($\text{Tm}_3\text{Fe}_5\text{O}_{12}$, TmIG), has been engineered into a binary memory with robust perpendicular magnetic anisotropy [9,10]. Additionally, TmIG thin films can exhibit a topological magnetic skyrmion phase [11,12],

which is promising for future magnetic insulator-based racetrack memory devices. Besides these promising practical applications, magnetic insulators are well-known for hosting novel quantum phases such as Bose-Einstein condensate [13–15], spin superfluidity [16–18], and topological magnonic insulators [19].

Magnetic heterostructures can provide additional functionalities and richer properties because exchange interactions between different layers provide another control mechanism [20,21]. While ferromagnetic metal-based heterostructures have been extensively studied and applied in commercial devices, such as magneto-resistive random-access memory [21,22], magnetic insulator-based heterostructures are still on the horizon yet have already showcased a few promising properties, including strong interfacial couplings [23–27], magnon valve effects [28–30], control of magnon transport in the magnetic insulator layer using another magnetic layer [31,32], magnonic crystals [33,34], coherent magnon-magnon couplings

*Contact author: zhwei@unc.edu

†Contact author: eeqshao@ust.hk

‡Equal contributions.

[35–38], and topological spin textures [12,19]. Magnetic insulator heterostructures are also theoretically predicted to host exotic topological magnonic insulator states [39,40]. However, to date, coherent magnon-magnon coupling has only been studied in hybrid systems consisting of low-damping YIG and another ferromagnetic metal [35–38]. The demonstration of low-damping and strong-coherent coupling in purely magnetic insulator bilayers remains lacking.

In this work, we demonstrate a low dissipation rate and a strong magnon-magnon coupling in a TmIG/YIG heterostructure. We characterize the structural and magnetic properties of our TmIG/YIG heterostructures on gadolinium gallium garnet ($\text{Gd}_3\text{Ga}_5\text{O}_{12}$, GGG) using high-angle annular dark-field scanning transmission electron microscopy (HAADF-STEM), x-ray diffraction (XRD), and vibrating sample magnetometry (VSM). Then, we investigate the magnetic dynamics in these bilayers by using a broadband ferromagnetic resonance (FMR) technique at room temperature. We observed a strong coupling between the Kittel mode of YIG and the perpendicular standing spin-wave (PSSW) mode of TmIG. By matching the experimental FMR spectra with analytical calculations and micromagnetic simulations, we obtain the exchange coupling strength at the interface, which is dependent on the magnetic insulator layer thickness and coupling mode. Finally, we benchmark the dissipation rates and cooperativity in our samples against those in ferromagnetic metal-based heterostructures.

II. RESULTS AND DISCUSSION

YIG, TmIG, and YIG/TmIG thin films were deposited on GGG(100)-single-crystal substrates by pulsed laser deposition (PLD). The films were deposited at 710 °C in an oxygen atmosphere of 100 mTorr, with a base pressure above 2×10^{-6} mTorr, using a 248 nm KrF excimer laser with 220 mJ energy and a repetition rate of 10 Hz. The deposition rates of YIG and TmIG thin films were calibrated by x-ray reflectivity to be about 6.89 nm/min and 7.13 nm/min, respectively. In-situ postannealing was carried out at the deposition temperature for 10 min in 10 Torr oxygen ambient, followed by natural cooling to room temperature. Each film has a normal area of $5 \times 5 \text{ mm}^2$. For comparison, we also deposited a 50-nm CoFeB ferromagnetic film on top of 350-nm TmIG using magnetron sputtering.

To assess the growth quality of the films, we conducted a series of material characterizations. Atomic images

from HAADF-STEM demonstrate a single crystallinity and perfect interfaces at the YIG/GGG and TmIG/YIG boundaries [Fig. 1(a)]. Elemental mapping [Fig. 1(b)] confirms there is no interdiffusion between different layers. Figure 1(c) presents the high-resolution XRD spectra of the TmIG/GGG, YIG/GGG, and TmIG/YIG/GGG bilayer films measured with the scattering vector normal to the (001)-orientation of the cubic substrate. Along the sharp (004)-peaks from the GGG substrate, the XRD spectra show Laue oscillations, indicating a smooth surface and interface.

We also measured the magnetic hysteresis loops for the YIG, TmIG, and TmIG/YIG samples to quantify their saturation magnetizations [Fig. 2(a)]. In principle, the exchange coupling strength (J) between different layers can be estimated from major and minor hysteresis loops [21]. However, due to the similar coercivity of YIG and TmIG, we can only see an enhanced coercivity [41]. In contrast, we can observe an intermediate ferromagnetic state in the reference sample, CoFeB (50 nm)/TmIG (350 nm), where CoFeB and TmIG have different coercivities [Fig. 2(b)]. Two features indicate ferromagnetic (FM) coupling in the CoFeB/TmIG sample: first, all switching occurs within the CoFeB coercive field [Fig. 2(b)]; second, the TmIG minor loops have a smaller coercivity than the original TmIG [42–44]. We can estimate the interfacial exchange energy J at the CoFeB (50 nm)/TmIG (350 nm) interface by measuring the minor loops (Appendix A). We extract the J as 0.031 mJ/m², indicating a ferromagnetic exchange coupling.

We measure the magnetization dynamics in the TmIG (200 nm)/YIG (200 nm) bilayers using a field-modulated FMR technique (Appendix B). We mount the sample on a coplanar waveguide and apply a microwave current that generates radiofrequency magnetic fields [Fig. 3(a)]. The absorption coefficient exhibits a peak when the FMR conditions for YIG and TmIG are met [Fig. 3(b)]. We experimentally extract the resonance frequency at a specific field by fitting a frequency scan for the field using Lorentz functions [represented by dots in Fig. 4(a)]. In addition to regular FMR peaks, we also observe anticrossing at specific field-frequency points, which are signatures of exchange interaction-driven coupling of the Kittel mode in YIG and the PSSW modes in TmIG. To identify the underlying magnon modes responsible for the coupling, we apply the formula for generalized excited spin-wave modes in two layers ($(\omega_i/2\pi)$ or f_i) [45], i.e.,

$$\frac{\omega_i}{2\pi} = f_i = \frac{\gamma_i}{2\pi} \sqrt{\left(\mu_0 H_{\text{ext}} + \frac{2A_{\text{ex},i}}{M_{s,i}} k_i^2\right) \left(\mu_0 H_{\text{ext}} + \frac{2A_{\text{ex},i}}{M_{s,i}} k_i^2 + \mu_0 M_{\text{eff},i}\right)}, \quad (1)$$

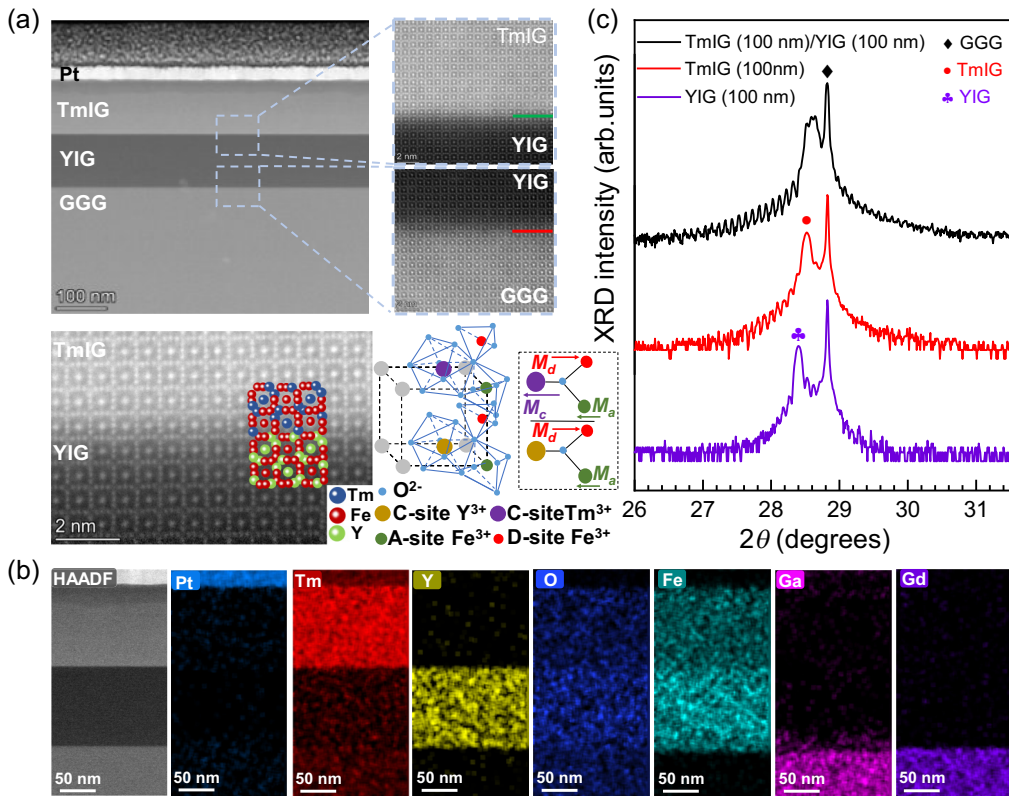


FIG. 1. Structural characterizations of the YIG/TmIG heterostructures on GGG substrates. (a) High-angle annular dark-field scanning transmission electron microscopy (HAADF-STEM) image of the YIG/TmIG heterostructure on GGG substrates. The YIG/GGG and YIG/TmIG interfaces are denoted by the green and red lines in the partially enlarged figure, respectively. Pt is used as a capping layer to prevent damage when preparing TEM samples. The inset of (a) demonstrates that two 1/8 of unit cells correspond to YIG and TmIG at the interface, which have the garnet-type structures $(C_3A)_2(D_3O_{12})$. (b) Energy dispersive x-ray spectra of different elements in the TmIG/YIG/GGG heterostructure. The images were taken along the $\langle 100 \rangle$ -direction of the GGG substrate, and the distribution of elements is marked in the figure with varying colors. (c) High-resolution x-ray diffraction spectra for the YIG (100 nm)/GGG, TmIG (100 nm)/GGG, and the TmIG (100 nm)/YIG (100 nm)/GGG samples.

where $i = \text{YIG}$ or TmIG , $\gamma_i/2\pi = 28(g_{\text{eff},i}/2)$ GHz/T is the gyromagnetic ratio, μ_0 is the permeability, H_{ext} is the external field, M_s is the effective magnetization, A_{ex} is the exchange stiffness, and k is the wavevector of the excited spin wave. Note that, when the resonance peaks are distant from the strong coupling region, the k value degenerates and tends toward the integer solutions 0, 1, 2, 3 (Appendix C); this means that we can fit the Kittel and PSSW modes through experimental data distant from the strong coupling region. We obtain $g_{\text{eff,YIG}} = 2$ ($\mu_0 M_{\text{eff,YIG}} = 0.25$ T) and $g_{\text{eff,TmIG}} = 1.56$ ($\mu_0 M_{\text{eff,TmIG}} = 0.24$ T) for YIG and TmIG, respectively, which are consistent with previous reports [46,47]. In addition, we determine the exchange stiffness of the TmIG to be 2.69 pJ/m through analyzing the higher-order mode, which is consistent with a previous report [48]. When the resonance field and frequency are near the strong coupling region, we expect an anticrossing gap, which can be described by the minimum frequency separation of $2g$. However, with only Eq. (1), the relation between the

exchange interaction and the g value cannot be uniquely determined.

To fully understand the exchange coupling-driven magnon-magnon coupling, we performed a comprehensive numerical analysis and micromagnetic simulations. For the COMSOL MICROMAGNETIC SIMULATION module [49], we solve the Landau-Lifshitz-Gilbert (LLG) equation by introducing the interfacial exchange-induced equivalent field, i.e.,

$$\mathbf{H}_{\text{ex, TmIG (YIG)}} = \frac{2J}{M_{\text{YIG}} + M_{\text{TmIG}}} \delta(z) \mathbf{m}_{\text{YIG (TmIG)}},$$

where $\delta(z)$ is an impulse function. The details are described in Appendix C. For the numerical analysis, we considered the effect of interfacial exchange energy at the interface ($z = 0$) and two free boundary conditions at the surfaces ($z = d_1$ or d_2). From this fact, we derived the following equation (Appendix C):

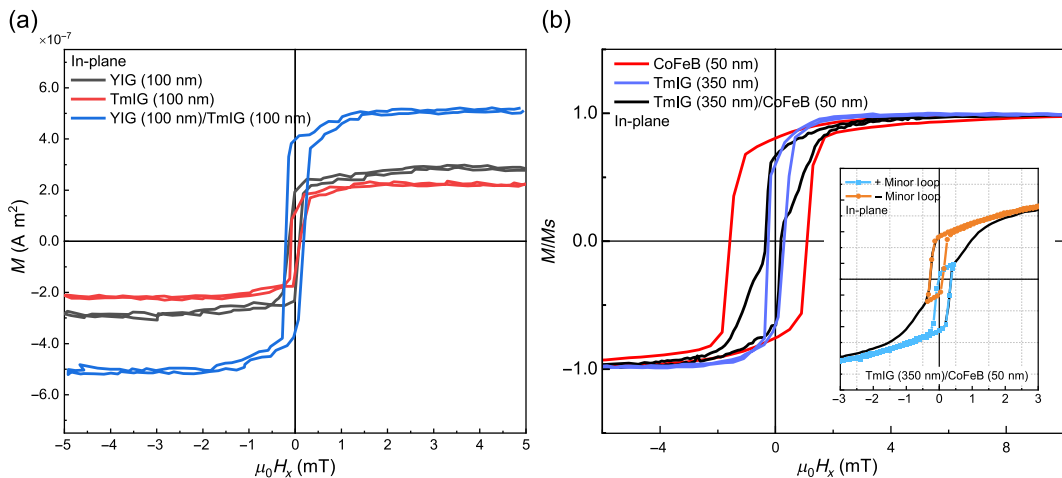


FIG. 2. Magnetic hysteresis loops for various samples. (a) Hysteresis loops for YIG (100 nm), TmIG (100 nm), and the YIG (100 nm)/TmIG (100 nm) samples. (b) Normalized hysteresis loops for TmIG (350 nm), CoFeB (50 nm), and the TmIG(350 nm)/CoFeB (50 nm) samples, where the M_s of TmIG(350 nm) is $0.99 \times 10^{-6} \text{ A m}^2$, and the M_s of CoFeB(50 nm) is $1.50 \times 10^{-6} \text{ A m}^2$. The inset shows an enlarged detail of the hysteresis loop and minor loops for the TmIG (350 nm)/CoFeB (50 nm) heterostructure sample.

$$\frac{2A_{\text{ex}, \text{YIG}}}{M_{s, \text{YIG}}} k_{\text{YIG}} \tan(k_{\text{YIG}} d_{\text{YIG}}) \cdot \frac{2A_{\text{ex}, \text{TmIG}}}{M_{s, \text{TmIG}}} k_{\text{TmIG}} \tan(k_{\text{TmIG}} d_{\text{TmIG}}) \\ = \frac{2J}{\mu_0(M_{s, \text{YIG}} + M_{s, \text{TmIG}})} \left[\frac{2A_{\text{ex}, \text{YIG}}}{M_{s, \text{YIG}}} k_{\text{YIG}} \tan(k_{\text{YIG}} d_{\text{YIG}}) + \frac{2A_{\text{ex}, \text{TmIG}}}{M_{s, \text{TmIG}}} k_{\text{TmIG}} \tan(k_{\text{TmIG}} d_{\text{TmIG}}) \right], \quad (2)$$

where J is the interfacial exchange energy. By solving $\omega_{\text{YIG}} = \omega_{\text{TmIG}}$ from Eqs. (1) and (2) combined, we can obtain a set of $(k_{\text{YIG}}, k_{\text{TmIG}})$ values that correspond to

different modes. In the presence of exchange interactions near the strong coupling region, k will not be precisely equal to $n\pi/d$ anymore. As a result, the degeneracy

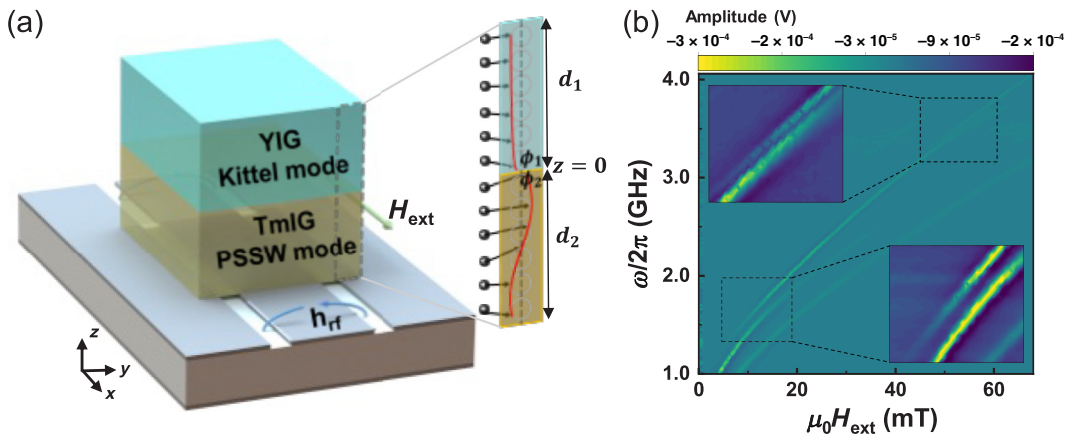


FIG. 3. Schematic diagram of the spin waves in the heterostructure and the measured resonance spectra. (a) Schematic illustration of the measurement set-up, where h_{rf} and H_{ext} stand for the microwave magnetic field and external static magnetic field, respectively. Spin-wave spectra are obtained by placing the sample face-down on a coplanar waveguide (CPW). The inset depicts the Kittel uniform spin-wave mode in the YIG and the perpendicular standing spin-wave (PSSW) mode in the TmIG. (b) Experimentally obtained color-coded spin-wave absorption spectra of the YIG (200 nm)/TmIG (200 nm) for the first three resonance modes of TmIG ($n = 0, 1, 2$) and the uniform mode of YIG ($n = 0$).

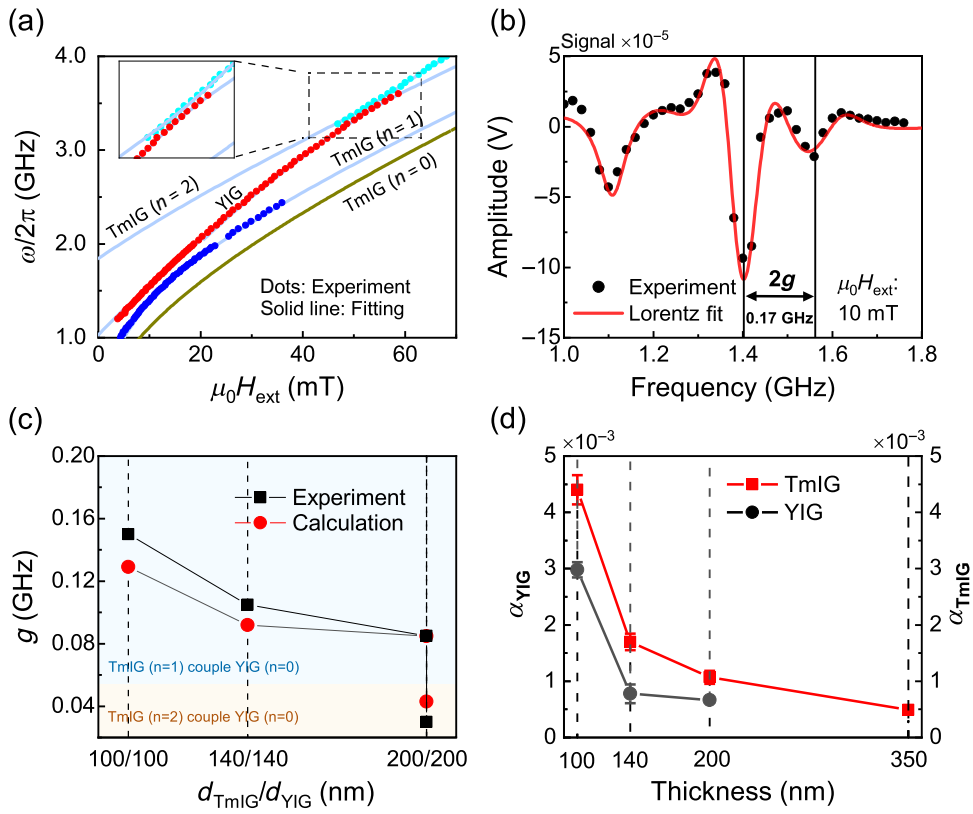


FIG. 4. Observation of strong magnon-magnon coupling and low damping in the YIG/TmIG bilayers. (a) Resonant absorption peaks of the two hybrid modes as a function of the external magnetic field with the YIG (200 nm)/TmIG (200 nm) bilayer. Solid lines show the numerical theory method fitting for hybrid modes. Data points are extracted from experimental data by reading out the minimum of each resonant peak from Fig. 3(b). (b) Spin-wave spectra at the minimum resonance separation ($\mu_0 H_{\text{ext}} = 10 \text{ mT}$) in magnetic insulator bilayers with the YIG (200 nm)/TmIG (200 nm) bilayer. (c) Coupling strength g between the TmIG($n=1,2$) mode and YIG ($n=0$) mode as a function of the YIG thickness. Black squares represent experimental results and red circles signify results from theoretical calculations. (d) Thickness dependence of Gilbert damping factors YIG and TmIG in the TmIG-based bilayers.

is lifted at the crossing point, resulting in two distinct frequencies, each corresponding to a different pair of wave vectors, k_{YIG} and k_{TmIG} . By employing $J = -0.057 \text{ mJ/m}^2$ (Table II), we have obtained high consistency between the experimental and calculated spectra of field-frequency points in the entire range [Fig. 4(a)]. The negative sign suggests an antiferromagnetic exchange coupling between TmIG and YIG. The strength is also comparable with that of the ferromagnetic metal/YIG bilayers [35]. We have also conducted the FMR measurement on the reference TmIG(350 nm)/CoFeB(50 nm) sample (Appendix D). We obtain $J = 0.0421 \text{ mJ/m}^2$, which is close to the result from the VSM loop measurements. This consistency suggests that we can reliably extract the J values of the TmIG/YIG samples from the FMR measurement.

We further study the thickness and mode dependence of the anticrossing gap ($2g$). We extract the g value from the frequency scan; for example, $g = 85 \text{ MHz}$ for the TmIG(200 nm)/YIG(200 nm) bilayer [Fig. 4(b)]. We find that the gap reduces as the layer thickness increases

[Fig. 4(c)]. To understand this, we derive the following approximate solution (Appendix E):

$$g \approx \frac{\gamma_{\text{YIG}} \gamma_{\text{TmIG}}}{4\pi^2} \frac{|J|}{(M_s, \text{YIG} + M_s, \text{TmIG})} \cdot \frac{\sqrt{(2\mu_0 H_{\text{res}} + \mu_0 M_{\text{eff}}, \text{YIG})(2\mu_0 H_{\text{res}} + \mu_0 M_{\text{eff}}, \text{TmIG})}}{f_{\text{res}}} \cdot \frac{1}{\sqrt{d_{\text{YIG}} d_{\text{TmIG}}}}, \quad (3)$$

where ω_{res} and H_{res} are the resonance frequency and field in the gap center, respectively. The calculated results show the same trend as in the experiments [Fig. 4(c)]. Moreover, Eq. (3) allows us to analyze the g value for the coupling of the YIG Kittel mode to different TmIG PSSW modes. We compare the experimental and calculated g values for the coupling of $n=0$ mode in YIG and $n=2$ mode in TmIG in Fig. 4(c), which confirms that higher mode coupling results in a lower g in our case.

TABLE I. Summary of the dissipation rates, damping factors, coupling strengths, cooperativities, and interfacial exchange energy in the studied bilayers and some reported YIG/ferromagnetic metal (FM) bilayers that show magnon-magnon coupling.

Material 1/Material 2	$\kappa_1(\alpha_1)$	$\kappa_2(\alpha_2)$	g (GHz)	C	J (mJ/m ²)
YIG (100 nm)/TmIG (100 nm) (this work)	0.058 GHz $(2.98 \times 10^{-3} \pm 1.4 \times 10^{-4})$	0.046 GHz $(4.4 \times 10^{-3} \pm 3 \times 10^{-4})$	0.155	8.76	-0.0618
YIG (140 nm)/TmIG (140 nm) (this work)	0.0185 GHz $(7.78 \times 10^{-4} \pm 1.7 \times 10^{-4})$	0.054 GHz $(1.69 \times 10^{-3} \pm 2 \times 10^{-4})$	0.105	11.04	-0.0720
YIG (200 nm)/TmIG (200 nm) (this work)	0.01 GHz $(6.64 \times 10^{-4} \pm 4.2 \times 10^{-5})$	0.0295 GHz $(1.07 \times 10^{-3} \pm 1 \times 10^{-4})$	0.085	24.49	-0.0573
TmIG (350 nm)/CoFeB (50 nm) (this work)	0.0255 GHz $(4.91 \times 10^{-4} \pm 8 \times 10^{-5})$	0.232 GHz $(3 \times 10^{-3} \pm 3.9 \times 10^{-5})$	0.263	11.69	0.0421
YIG (20 nm)/Ni (20 nm) [37]	0.06 GHz	0.63 GHz	0.12	0.38	-
YIG (20 nm)/Co (30 nm) [37]	0.06 GHz	0.5 GHz	0.79	21	-
YIG (100 nm)/Ni ₈₀ Fe ₂₀ (9 nm) [35]	0.106 GHz (2.3×10^{-4})	0.192 GHz (1.75×10^{-3})	0.35	6	-0.060 ± 0.011

Finally, to evaluate the coupling cooperativity in the TmIG/YIG bilayers, we determined the damping factors and individual dissipation rates. The damping factor is determined by the frequency-dependent field linewidth in the field scans, and the dissipation rate is found by directly measuring the frequency linewidth in the frequency scans. The relation between the damping and dissipation rate is given by [50]

$$\Delta f = (\gamma \Delta H_0 + 4\pi \alpha f) \sqrt{1 + \left(\frac{\gamma \mu_0 M_s}{4\pi f} \right)^2}, \quad (4)$$

where ΔH_0 is inhomogeneous broadening. From Eq. (4), we can see that a lower M_s is preferred for realizing a lower dissipation rate given the same damping factor. In this sense, magnetic insulators have lower dissipation rates, which justifies the widespread usage of YIG for coherent magnonics.

We experimentally determine the Gilbert damping factors for YIG and TmIG from field scans at different frequencies when they are not coupled (Appendix E). The extracted damping factors are plotted in Fig. 4(d), where we find a damping factor as low as $4.91 (\pm 0.79) \times 10^{-4}$ in the 350-nm-thick TmIG. Note that in the coupled regime, we observe a crossover of damping coefficients for the two modes (Fig. 15), indicating a mutual spin pumping-induced dampinglike torque effect [35]. We also extract the dissipation rates for YIG and TmIG from frequency scans at different fields when they are not coupled (Appendix F). As an example, $\kappa_{\text{YIG}} = 10$ MHz and $\kappa_{\text{TmIG}} = 29.5$ MHz for the TmIG(200 nm)/YIG(200 nm) bilayer. Therefore, $g > \kappa_{\text{YIG}}, \kappa_{\text{TmIG}}$, and

$$C = \frac{g^2}{\kappa_{\text{YIG}} \kappa_{\text{TmIG}}} = 24.5,$$

denoting a strong coupling behavior in the bilayer. In Table I, we summarize the dissipation rates and cooperativity for TmIG- and ferromagnetic metal-based heterostructures that show magnon-magnon coupling. The TmIG has a very low dissipation rate compared with the ferromagnetic metals, which is consistent with a low Gilbert damping.

III. CONCLUSION

In summary, we demonstrate low damping and dissipation rates in TmIG and achieve strong magnon-magnon coupling and high cooperativity in the TmIG/YIG bilayers. The combined experimental and theoretical analyses allow us to determine the interfacial exchange coupling strengths in our all-insulator bilayers. The all-magnetic-insulator bilayers allow us to achieve low-damping insulating magnonic crystals and other artificial structures to realize energy-efficient spin-wave devices. In particular, we highlight that our YIG/TmIG single crystalline heterostructure is a better choice than the originally proposed YIG/permalloy (Py, NiFe) heterostructure for constructing a topological magnonic insulator [39], where Py is amorphous and has a high dissipation rate. Importantly, this choice enables the realization of nontrivial states within more practical magnon wavevector ($k \sim 10^7$ m⁻¹) and frequency ($f \sim 9$ GHz) ranges that align with the majority of magnon-based computing and signal transmission experiments, avoiding the challenges associated with high-frequency ($f \sim 51$ GHz) microwave measurements and the limited $k \sim 10^8$ m⁻¹ values suitable for YIG/Py systems (Appendix G).

Note that, very recently, Y. Li *et al.* independently reported reconfigurable magnon-magnon coupling in

hybrid ferrimagnetic insulators YIG/Gd₃Fe₅O₁₂ (GdIG) by varying the temperature [51].

ACKNOWLEDGMENTS

The authors appreciate insightful discussions with S. S. Kim, Y. Tserkovnyak, Z. Zhang, A. Comstock, D. Sun, and Y. Li. The sample fabrication, structural characterization, and data analysis at HKUST were supported by the National Key R&D Program of China (Grant No. 2021YFA1401500) and the RGC General Research Fund (Grant No. 16303322). The magnetic dynamics measurement and analysis were supported by the U.S. National Science Foundation under Grant No. ECCS-2246254. The authors also acknowledge support from the RGC General Research Fund (Grant No. 16303322), the State Key Laboratory of Advanced Displays and Optoelectronics Technologies (HKUST), and the Guangdong-Hong Kong-Macao Joint Laboratory for Intelligent Micro-Nano Optoelectronic Technology (Grant No. 2020B1212030010).

APPENDIX A: ESTIMATION OF INTERFACIAL EXCHANGE ENERGY IN TmIG/CoFeB SAMPLE BY MINOR LOOPS

Subsequently, to quantify the interfacial exchange field and energy, we measured the minor hysteresis loops of TmIG(350 nm)/CoFeB(50 nm), as shown in Fig. 5(a). In an ideal state, states (2) and (3) are similar, but the difference is that the moment in state (3) is about to flip the spin of the TmIG layer, and the moment of state (2) has not yet reached the flip condition. The – minor loop measured from the experiment is a C–A–B–C loop [Fig. 5(b)], indicating the existence of ferromagnetic interfacial coupling. If there were no interfacial coupling, the loop would resemble something similar to E–A–D–E because it would depend on the coercivity of TmIG; that is, the forward and reverse minor loops should basically coincide (just like a single TmIG hysteresis loop). The shift in the minor hysteresis loops is precisely due to the interfacial exchange coupling; the two layers are in a ferromagnetic relationship such that the extra H_{ex} wants to align the spins parallel, which is why the flipping in state (3) will be faster by ($H_{\text{ex}} - H_{\text{ext}}$). Thus, we can estimate the interfacial exchange energy J value from the minor loops:

$$J = \mu_0 H_{\text{ex}} \frac{\Delta M_s}{V} t = 0.394 \times 10^{-3} (\text{T}) \times 1.975 \times 10^5 (\text{A/m}) \times 400 \times 10^{-9} (\text{m}) = 0.03113 \text{ mJ/m}^2,$$

where H_{ex} is the exchange field induced by the interfacial coupling, ΔM_s is the value of magnetization reduction in the shadow region (C–B–D–E loop) due to the additional exchange field, $V = (350 \text{ nm} + 50 \text{ nm}) \times 5 \text{ mm} \times 5 \text{ mm}$ is the volume of the heterostructure, and t is the thickness

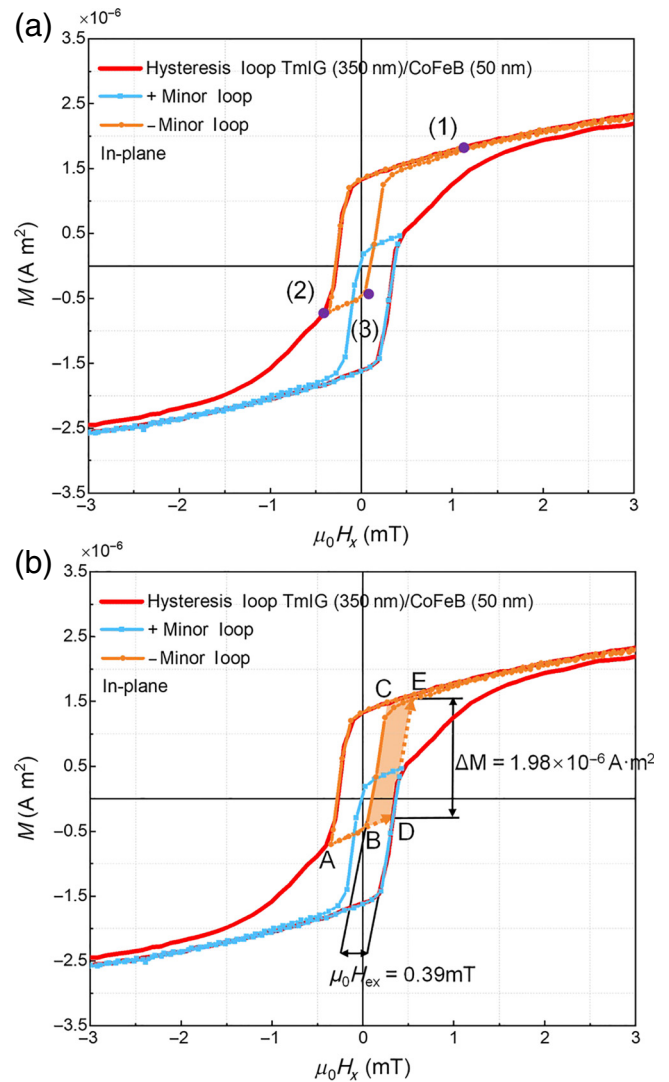


FIG. 5. Hysteresis loop and minor loops for the TmIG(350 nm)/CoFeB(50 nm) sample. (a) Minor loops for the TmIG(350 nm)/CoFeB(50 nm) sample. The noncoincidence of the + minor loop and the – minor loop indicates the existence of interfacial coupling. (b) Process of analyzing interfacial exchange coupling using minor loops. The result of the experimental measurement is a C–A–B–C loop, indicating the existence of ferromagnetic interfacial coupling. However, if there is no interfacial exchange coupling, the loop would be similar to E–A–D–E because it only depends on the coercivity of TmIG; that is, the forward and reverse minor loops should basically coincide (just like an individual TmIG hysteresis loop). We can also obtain comparable results from the + minor loop using a similar method.

of the sample. After analyzing the interfacial exchange coupling by the minor loops, we also extracted the interfacial coupling energy of the TmIG(350 nm)/CoFeB(50 nm) sample by ferromagnetic resonance (FMR) measurement, as detailed in Appendix C.

APPENDIX B: RESONANCE STUDY

The magnetization dynamics measurement was performed using the field-modulation FMR technique at room temperature. During the measurement, the GGG/YIG/TmIG sample was mounted in the flip-chip configuration (TmIG side facing down) on top of the signal line of a coplanar waveguide for broadband microwave excitation. An external bias field, H , was applied in a plane perpendicular to the rf field of the coplanar waveguide (CPW). We used a modulation frequency of $\Omega/2\pi = 81.57$ Hz (supplied by a lock-in amplifier and provided by a pair of modulation coils) and a modulation field of about 1.1 Oe. The microwave signal was delivered from a signal generator (0–5 dBm) to one port of the board. The field-modulated FMR signal was measured from the other port by the lock-in amplifier in the form of a DC voltage, V , by using a sensitive rf diode. We swept the bias field, H , and at each incremental frequency, f , to construct the $V[f, H]$ dispersion contour plots. The FMR spectral lines are fitted using the superposition of Lorentzian and anti-Lorentzian functions:

$$\begin{aligned} \frac{dP}{dH_{DC}} = & K1 \frac{4\Delta H(H - H_{res})}{[4(H - H_{res})^2 + (\Delta H)^2]} \\ & - K2 \frac{\Delta H^2 - 4(H - H_{res})^2}{[4(H - H_{res})^2 + (\Delta H)^2]} \\ & + \text{slope}(H) + \text{offset} \end{aligned} \quad (B1)$$

APPENDIX C: NUMERICAL ANALYSIS AND MICROMAGNETIC SIMULATION FOR THE STRONG MAGNON-MAGNON COUPLING INDUCED BY THE INTERFACE EXCHANGE INTERACTION

1. Numerical analysis

We conducted a numerical analysis and micromagnetic simulations on the bilayer heterostructure following the method in refs. [35,52]. We assume that magnetic insulator layer 1 (MI1) and magnetic insulator layer 2 (MI2) are represented by indexes 1 and 2, respectively. The interface of the MI1 and MI2 is at $z = 0$ [Fig. 6(a)].

2. Dispersion relation

For the magnetic system, the Landau-Lifshitz-Gilbert (LLG) equation [Eq. (C1)] describes the intrinsic precession of the spin in the materials

$$\frac{\partial \vec{M}_i}{\partial t} = -\mu_0 \gamma_i \vec{M}_i \times \vec{H}_{\text{eff},i} + \frac{\alpha_i}{M_{s,i}} \left(\vec{M}_i \times \frac{\partial \vec{M}_i}{\partial t} \right), \quad (C1)$$

where the whole magnetic insulator bilayers are subjected to the static magnetic field \vec{H}_{ext} in the x -direction and the dynamic magnetic field \vec{h}_{rf} generated by the

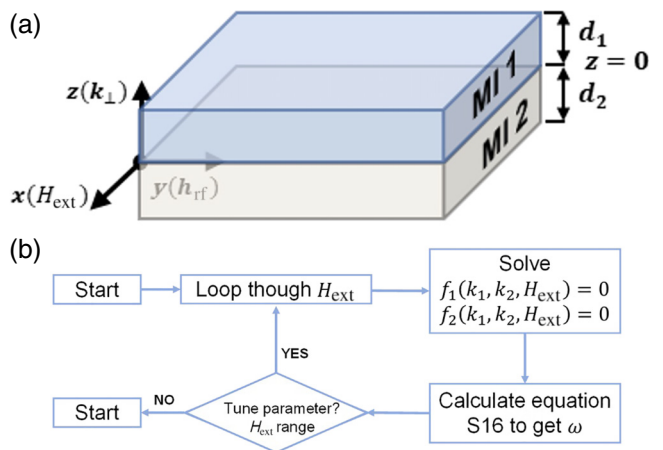


FIG. 6. (a) Schematic of the magnetic insulator heterostructure with thicknesses d_1 and d_2 . For convenience of calculation, we set the interface of the bilayer as the interface of $z = 0$. The direction of the static external magnetic field (H_{ext}) is set as the x -axis, and the dynamic magnetic field (h_{rf}) generated by CPW is perpendicular to the static magnetic field on the y -axis, where $H_{\text{ext}} \gg h_{\text{rf}}$. (b) Theoretical calculation framework from MATLAB. We traverse the value of H_{ext} through the loop cycle and solve Eqs. (C13) and (C23) under each external magnetic field value to obtain the k_1 and k_2 , then substitute them into the dispersion relationship to obtain the eigenfrequencies.

coplanar waveguide (CPW) in the y -direction. Since the dynamic magnetic field induced by the microwave is so small ($|\vec{h}_{\text{rf}}| \ll |\vec{H}_{\text{ext}}|$), the precessing amplitude of the spin moment can be divided into static and dynamic parts, i.e.,

$$\begin{aligned} \vec{M}_i &= M_{s,i}(\vec{m}_{0,i} + \delta \vec{m}_i), \quad \vec{m}_{0,i} \\ &= \begin{bmatrix} 1 \\ 0 \\ 0 \end{bmatrix}, \quad \delta \vec{m}_i = \delta \vec{m}_{0,i} e^{j\omega t} = \begin{bmatrix} \delta m_{x,i} \\ \delta m_{y,i} \\ \delta m_{z,i} \end{bmatrix}, \end{aligned} \quad (C2)$$

where \vec{m}_0 is a normalization constant modulo 1, which is the static expression of the spin moment. Moreover, $\delta \vec{m}_i$ is a microperturbation induced by microwave fields; its amplitude is much smaller than $|\vec{m}_0|$. In addition, \vec{H}_{eff} includes an external magnetic static magnetic field \vec{H}_{ext} [Eq. (C3)] in the x -direction, the dynamic magnetic field is \vec{h}_{rf} , $|\vec{h}_{\text{rf}}| \ll |\vec{H}_{\text{ext}}|$, $\vec{h}_{\text{rf}} \perp \vec{H}_{\text{ext}}$, and the demagnetization field is $\vec{H}_{\text{de},i}$ [Eq. (C4)]. In particular, the sample is considered as a thin film, so that $N_x = N_y = 0$, $N_z = 1$, and the demagnetization field could be described by $\vec{H}_{\text{de},i} = -\mu_0 M_{s,i}(0, 0, \delta m_{z,i})$. The following can be determined:

$$\vec{H}_{\text{ext}} = \begin{bmatrix} H_x \\ 0 \\ 0 \end{bmatrix}, \quad \vec{m}_{0,i} \parallel \vec{H}_{\text{ext}}. \quad (C3)$$

Substitute \vec{M}_i and $\vec{H}_{\text{eff},i}$ into Eq. (C1), we find

$$\begin{aligned} M_{s,i} \frac{\partial(\vec{m}_{0,i} + \delta\vec{m}_i)}{\partial t} &= -\mu_0 \gamma_i M_{s,i} (\vec{m}_{0,i} + \delta\vec{m}_i) \times (\vec{H}_{\text{ext}} + \vec{H}_{\text{de}} + \vec{h}_{\text{rf}}) \\ &\quad + \frac{\alpha_i}{M_{s,i}} M_{s,i} (\vec{m}_{0,i} + \delta\vec{m}_i) \times M_{s,i} \frac{\partial(\vec{m}_{0,i} + \delta\vec{m}_i)}{\partial t}, \end{aligned} \quad (\text{C4})$$

where $\partial\vec{m}_{0,i}/\partial t = 0$ and $\partial\delta\vec{m}_i/\partial t = j\omega\delta\vec{m}_i e^{j\omega t} = j\omega\delta\vec{m}_i$. In Eq. (C4), $\vec{m}_{0,i} \times \vec{H}_{\text{ext}} = 0$ due to the fact that the magnetization and the static component of the external magnetic field are parallel to each other; $\delta\vec{m}_i \times \vec{h}_{\text{rf}} = 0$ is because of the second-order epsilon and $\delta\vec{m}_i \times \partial\delta\vec{m}_i/\partial t = \delta\vec{m}_i \times j\omega\delta\vec{m}_i = 0$. So, Eq. (C4) could be simplified to

$$j\omega\delta\vec{m}_i = -\mu_0 \gamma_i (\vec{m}_{0,i} \times \vec{H}_{\text{de}} + \vec{m}_{0,i} \times \vec{h}_{\text{rf}} + \delta\vec{m}_i \times \vec{H}_{\text{ext}}) + j\omega\alpha_i (\vec{m}_{0,i} \times \delta\vec{m}_i). \quad (\text{C5})$$

The matrix form of Eq. (C5) is given by

$$j\frac{\omega}{\mu_0\gamma_i} \begin{bmatrix} \delta m_{x,i} \\ \delta m_{y,i} \\ \delta m_{z,i} \end{bmatrix} = - \left[\begin{bmatrix} 0 \\ M_{s,i}\delta m_{z,i} \\ 0 \end{bmatrix} + \begin{bmatrix} 0 \cdot h_x \\ -h_z \\ h_y \end{bmatrix} + \begin{bmatrix} 0 \\ H_x\delta m_z \\ -H_x\delta m_y \end{bmatrix} \right] + j\frac{\omega\alpha_i}{\mu_0\gamma_i} \begin{bmatrix} 0 \\ -\delta m_z \\ \delta m_y \end{bmatrix}. \quad (\text{C6})$$

Simplify Eq. (C6) into $\vec{h} = \chi^{-1}\delta\vec{m}$, we find

$$\begin{bmatrix} 0 \cdot h_x \\ h_y \\ h_z \end{bmatrix} = \begin{bmatrix} j\frac{\omega}{\mu_0\gamma_i} & 0 & 0 \\ 0 & \left(H_x + j\frac{\omega\alpha_i}{\mu_0\gamma_i}\right) & -j\frac{\omega}{\mu_0\gamma_i} \\ 0 & j\frac{\omega}{\mu_0\gamma_i} & \left(M_s + H_x - j\frac{\omega\alpha_i}{\mu_0\gamma_i}\right) \end{bmatrix} \begin{bmatrix} \delta m_{x,i} \\ \delta m_{y,i} \\ \delta m_{z,i} \end{bmatrix}. \quad (\text{C7})$$

When the FMR condition is met, the system reaches a maximum resonance, meaning that the system, with $\vec{h} = 0$ and $\chi^{-1}\vec{m} = 0$, has a nonzero solution [Eq. (C8)] so that

$$|\chi^{-1}| = 0, \quad (\text{C8})$$

$$(1 - \alpha_i^2)\omega^2 - j\mu_0\gamma_i M_{s,i}\alpha_i\omega - \mu_0^2\gamma_i^2 H_x (H_x + M_{s,i}) = 0, \quad (\text{C9})$$

$$\omega_{\text{complex}} = j\frac{\mu_0\gamma_i M_{s,i}\alpha_i}{2(1 - \alpha_i^2)} + \frac{1}{2(1 - \alpha_i^2)} \sqrt{\mu_0^2\gamma_i^2 M_{s,i}^2\alpha_i^2 + 4(1 - \alpha_i^2)[\mu_0^2\gamma_i^2 H_{x,i}(H_{x,i} + M_{s,i})]}. \quad (\text{C10})$$

Equation (C10) is a Kittel mode by solving the linearized LLG equation with a wave vector $k = 0$. If we consider the exchange field $\vec{H}_{\text{ex}} = (2A_{\text{ex},i}/M_{s,i})k_i^2$, the Eq. (C11) can be revised to be the following:

$$\begin{aligned} \omega_{\text{complex}} &= j\frac{\mu_0\gamma_i M_{s,i}\alpha_i}{2(1 - \alpha_i^2)} \\ &\quad + \frac{1}{2(1 - \alpha_i^2)} \sqrt{\mu_0^2\gamma_i^2 M_{s,i}^2\alpha_i^2 + 4(1 - \alpha_i^2)\gamma_i^2 \left[\left(\mu_0 H_x + \frac{2A_{\text{ex},i}}{M_{s,i}} k_i^2\right) \left(H_{x,i} + \frac{2A_{\text{ex},i}}{M_{s,i}} k_i^2 + M_{s,i}\right) \right]}. \end{aligned} \quad (\text{C11})$$

When $\alpha \ll 1$, Eq. (C11) can be simplified to

$$\omega_i = \gamma_i \sqrt{\left(\mu_0 H_x + \frac{2A_{\text{ex},i}}{M_{s,i}} k_i^2\right) \left(\mu_0 H_x + \frac{2A_{\text{ex},i}}{M_{s,i}} k_i^2 + \mu_0 M_{s,i}\right)}, \quad (\text{C12})$$

where k_i is the wave vector of the perpendicular standing spin wave (PSSW) and the propagation of the spin wave is in the z -direction. In addition,

$$\omega_1 - \omega_2 = 0. \quad (\text{C13})$$

For the magnetic insulator bilayer, Eq. (C11) with α and Eq. (C12) without α describe the dispersion relation within each layer. Equation (C13) indicates the necessary condition for the bilayer spin waves to exist simultaneously under the same external condition (same h_{rf} and H_{ext}) in the two layers.

3. Boundary conditions—free boundary condition and interface exchange boundary condition

For the magnetic insulator bilayer system, the free boundary condition should be applied to the top ($z = d_1$) [Eq. (C14)] and the bottom ($z = -d_2$) [Eq. (C15)] of the bilayer system, which also means no pinning at the surfaces, i.e.,

$$\left. \frac{\partial \delta m_{z,1}}{\partial z} \right|_{z=d_1} = 0, \quad (\text{C14})$$

$$\left. \frac{\partial \delta m_{z,2}}{\partial z} \right|_{z=-d_2} = 0. \quad (\text{C15})$$

Considering that the dynamic magnetization in the x and y directions is uniform, there is a wave vector (k_{\perp}) along the thickness direction. The spatial distribution of the PSSW can be expressed as follows:

$$\delta m_{z,i} = \delta m_{0,i} \cos(k_i z + \phi_i), \quad (\text{C16})$$

where ϕ_i is the phase of the spin wave. By substituting Eq. (16) into Eqs. (C14) and (C15), we can obtain

$$-k_1 d_1 + n_1 \pi = \phi_1, \quad (\text{C17})$$

$$k_2 d_2 + n_2 \pi = \phi_2. \quad (\text{C18})$$

The interface exchange energy J describes the number and strength of the exchange bonds between magnetic insulator layer 1 and layer 2. The effect of interface exchange energy J (mJ/m^2) at the interface ($z = 0$) can be demonstrated by the interface boundary conditions generated by the combination of the Huffman boundary conditions [53]. The conservation of magnetic energy flow at the interface leads to

$$\left. \frac{2A_{\text{ex},1}}{M_{s,1}} \frac{\partial \delta m_{z,1}}{\partial z} + \frac{2J}{(M_{s,1} + M_{s,2})} (\delta m_{z,2} - \delta m_{z,1}) \right|_{z=0} = 0, \quad (\text{C19})$$

$$\left. -\frac{2A_{\text{ex},2}}{M_{s,2}} \frac{\partial \delta m_{z,2}}{\partial z} + \frac{2J}{(M_{s,1} + M_{s,2})} (\delta m_{z,1} - \delta m_{z,2}) \right|_{z=0} = 0. \quad (\text{C20})$$

The matrix form of Eqs. (C19) and (C20) is as follows:

$$\begin{bmatrix} 0 \\ 0 \end{bmatrix} = \begin{bmatrix} -\frac{2J}{(M_{s,1} + M_{s,2})} \cos \phi_1 - \frac{2A_{\text{ex},1}}{M_{s,1}} k_1 \sin \phi_1 & \frac{2J}{(M_{s,1} + M_{s,2})} \cos \phi_2 \\ \frac{2J}{(M_{s,1} + M_{s,2})} \cos \phi_1 & -\frac{2J}{(M_{s,1} + M_{s,2})} \cos \phi_2 + \frac{2A_{\text{ex},2}}{M_{s,2}} k_2 \sin \phi_2 \end{bmatrix} \begin{bmatrix} \delta m_{0,1} \\ \delta m_{0,2} \end{bmatrix}. \quad (\text{C21})$$

The resonant condition requires that the determinant of the coefficient matrix of Eq. (C21) vanishes so that

$$\begin{aligned} & \left[\frac{2J}{(M_{s,1} + M_{s,2})} \cos \phi_1 + \frac{2A_{\text{ex},1}}{M_{s,1}} k_1 \sin \phi_1 \right] \left[\frac{2J}{(M_{s,1} + M_{s,2})} \cos \phi_2 - \frac{2A_{\text{ex},2}}{M_{s,2}} k_2 \sin \phi_2 \right] \\ &= \left[\frac{2J}{(M_{s,1} + M_{s,2})} \cos \phi_2 \right] \left[\frac{2J}{(M_{s,1} + M_{s,2})} \cos \phi_1 \right]. \end{aligned} \quad (\text{C22})$$

Equation (C22) is the relationship under the interface-exchanged boundary conditions. Combined with the free boundary conditions of Eqs. (C17) and (D18), we can obtain

$$\frac{2A_{\text{ex},1}}{M_{s,1}} k_1 \tan(k_1 d_1) \frac{2A_{\text{ex},2}}{M_{s,2}} k_2 \tan(k_2 d_2) = \frac{2J}{(M_{s,1} + M_{s,2})} \left[\frac{2A_{\text{ex},1}}{M_{s,1}} k_1 \tan(k_1 d_1) + \frac{2A_{\text{ex},2}}{M_{s,2}} k_2 \tan(k_2 d_2) \right]. \quad (\text{C23})$$

To obtain the eigenfrequency, we can solve the transcendental equations of the dispersion condition [Eq. (C13)] and boundary condition [Eq. (C23)] for each external magnetic field H_{ext} by traversal. Although $f_1(k_1, k_2, H_{\text{ext}}) =$

0 and $f_2(k_1, k_2, H_{\text{ext}}) = 0$ cannot be explicitly functionalized, we can solve them numerically by handling them as implicit functions. Figure 6(b) shows the framework of the numerical analysis using MATLAB software.

Next, we will solve the eigenfrequency for two cases ($J = 0 \text{ mJ/m}^2$ and $J \neq 0 \text{ mJ/m}^2$).

When $J = 0 \text{ mJ/m}^2$, transcendental Eq. (C23) degenerates to the following:

$$k_1 k_2 \tan(k_1 d_1) \tan(k_2 d_2) = 0, \quad (\text{C24})$$

where $k_1 = n\pi/d_1$ or $k_2 = n\pi/d_2$ is the solution of Eq. (C24), which means that the spin wave in magnetic insulator layer 1 and layer 2 is quantized as $n\pi/d$ and not influenced by each other. Substituting Eq. (C24) into Eq. (C12) (assuming that $\alpha \ll 1$), we find

$$\omega_i = \gamma_i \sqrt{\left(\mu_0 H_x + \frac{2A_{\text{ex},i}}{M_{s,i}} \left(\frac{n\pi}{d}\right)^2\right) \left(\mu_0 H_x + \frac{2A_{\text{ex},i}}{M_{s,i}} \left(\frac{n\pi}{d}\right)^2 + \mu_0 M_{s,i}\right)}. \quad (\text{C25})$$

To simplify our analysis and reduce the number of fitting parameters, we consider M_s and M_{eff} to be the same in the numerical analysis. The resonant peaks in

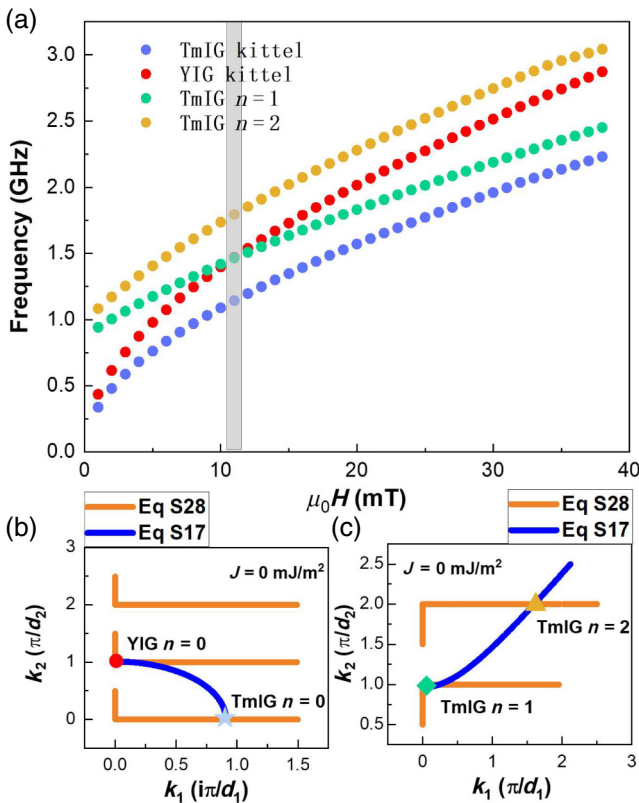


FIG. 7. Numerical solution for the eigenfrequency when $J = 0 \text{ mJ/m}^2$. (a) Frequencies of the FMR and PSSW modes of TmIG (200 nm) and FMR mode of YIG (200 nm) as a function of H when $J = 0 \text{ mJ/m}^2$. Numerical solutions obtained by solving the dispersion condition and boundary condition without interfacial exchange energy, where k_1 is a purely imaginary number (b) and a purely real number (c), respectively. When $J = 0 \text{ mJ/m}^2$, we can clearly see that the crossing points are a degenerate solution in the shaded region, which indicates that k_1 and k_2 are quantized solutions with $n\pi/d_1$ and $n\pi/d_2$, respectively.

Fig. 7(a) show the FMR and PSSW modes of TmIG and the FMR mode of YIG as a function of the magnetic field when $J = 0 \text{ mJ/m}^2$. We also demonstrate the process of

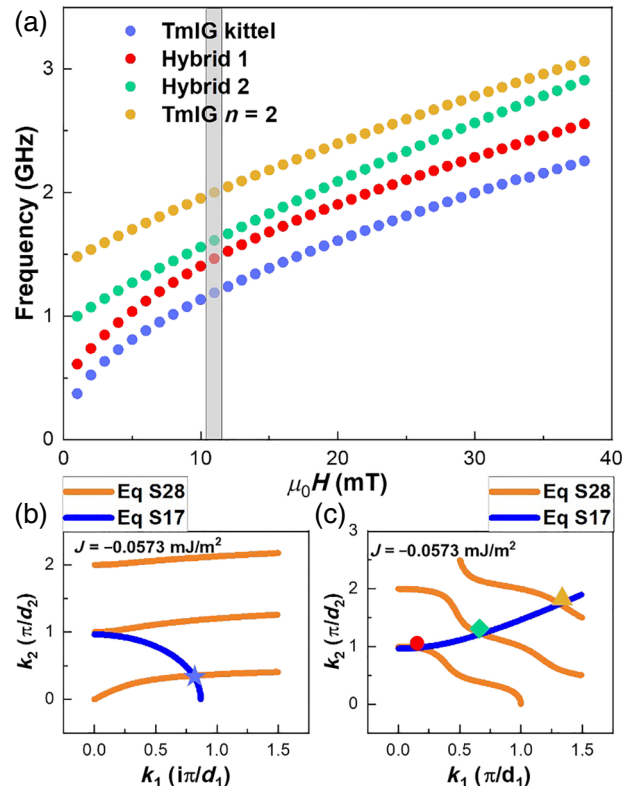


FIG. 8. Numerical solution for the eigenfrequency when $J = -0.0573 \text{ mJ/m}^2$. (a) Anticrossing coupling frequencies of hybrid modes of TmIG (200 nm)/YIG (200 nm) as a function of H when $J = -0.0573 \text{ mJ/m}^2$. Numerical solutions obtained by solving the dispersion condition and boundary condition with interfacial exchange energy, where k_1 is a purely imaginary number (b) and a purely real number (c), respectively we can see that the spin-wave vector solution is no longer $n\pi/d$. It is noted that the evanescent wave emerges in the YIG layer when the frequency of the PSSW in the TmIG layer is lower than the uniform mode in the YIG layer.

solving k_1 and k_2 using a graphical method, as in Figs. 7(b) and 7(c).

When $J \neq 0 = -0.0573 \text{ mJ/m}^2$, we can clearly see the anticrossing curve in Fig. 8(a). A set of degenerated solutions of the shaded region in Fig. 8(a) is composed of a set of intersection points from Figs. 8(b) and 8(c). It also needs to be noted that the evanescent wave emerges in the YIG layer when the frequency of the PSSW in the TmIG layer is lower than the uniform mode in the YIG layer (k_1 has a pure imaginary part).

4. Micromagnetic simulations

We apply the frequency-domain LLG equations, which are given as

$$-i\omega\delta\mathbf{m}_i = -\gamma_i\mathbf{m}_i \times \left(\mathbf{H}_{\text{eff}} + \frac{2J}{M_i + M_j} \delta(z)\mathbf{m}_j \right) - i\omega\alpha_i\mathbf{m}_i \times \delta\mathbf{m}_i, \quad (\text{C26})$$

$$-i\omega\delta\mathbf{m}_j = -\gamma_j\mathbf{m}_j \times \left(\mathbf{H}_{\text{eff}} + \frac{2J}{M_i + M_j} \delta(z)\mathbf{m}_i \right) - i\omega\alpha_j\mathbf{m}_j \times \delta\mathbf{m}_j, \quad (\text{C27})$$

to the two magnetic thin films, respectively. The simulation parameters that are set are shown in Table I. We characterize the strength of resonance through the response of δm_z to the magnetic field and microwave field. Through the simulation results shown in Fig. 9(a), we can clearly see that TmIG($n=1,2$) is coupled with YIG($n=0$) to form anticrossing at 10.5 mT and 47.0 mT. Figure 9(b) shows the spectral resonance curve of the spin wave at 10.5 mT. Then, we can observe the internal dynamics of spin waves through simulation. To demonstrate the resonance direction of the spin wave on the interface of the bilayers, we show the δm_z distribution of the normalized intensity in the z -direction for the two hybrid modes A and B (marked) in Fig. 10.

APPENDIX D: FMR VERIFICATION OF FERROMAGNETIC INTERFACIAL COUPLING ENERGY FOR THE TmIG(350 nm)/CoFeB(50 nm) SAMPLE

We also verify the ferromagnetic interfacial exchange energy of the MI/FM TmIG(350 nm)/CoFeB(50 nm) by FMR modulation. We use theory (Appendix C) to analyze and fit the color-coded experiment data [Figs. 11(a) and 11(b)] and obtain the TmIG/CoFeB interfacial coupling energy $J = 0.0421 \text{ mJ/m}^2$, showing that the FMR method is consistent with the minor hysteresis loop method ($J = 0.0311 \text{ mJ/m}^2$). We also extract the dissipation rate, Gilbert damping, and the coupling strength of the TmIG/CoFeB samples. The extraction method is the same as that of YIG/TmIG, as shown in Figs. 15–17 (Fig. 12).

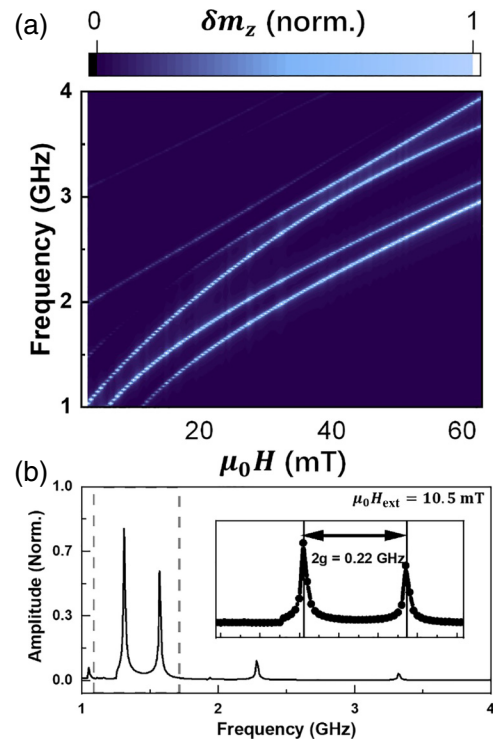


FIG. 9. Full micromagnetic simulation based on the frequency domain. (a) Color-coded spin-wave spectra with frequency and magnetic field with the TmIG (200 nm)/YIG (200 nm) heterostructure. We can clearly see that TmIG ($n=1,2$) is coupled with YIG ($n=0$) to form anticrossing at 10.5 mT and 47.0 mT. Then, we use the value of change in δm_z as the peak response. (b) Spin spectrum curve at the minimum resonance separation of the first anticrossing ($\mu_0 H_{\text{ext}} = 10.5 \text{ mT}$).

APPENDIX E: THICKNESS DEPENDENCE OF INTERFACIAL EXCHANGE COUPLING ENERGY AND COUPLING STRENGTH FOR TmIG/YIG SAMPLES

1. Sign judgment of interfacial exchange coupling energy

Judgment 1: we obtained the interfacial exchange energy ($J < 0 \text{ mJ/m}^2$) by fitting the experimental data with the theory of Appendix C. The values of the J are summarized in Table I. Judgment 2: We plot the spin-wave absorption spectra for TmIG(100 nm)/YIG(100 nm) in comparison with YIG(100 nm)/GGG (gray dashed line) in Fig. 13. The lower resonant magnetic field (H_{res}) or higher resonant frequency (ω_{res}) means that, for the TmIG/YIG sample, the interfacial exchange field applied on YIG is opposite to the external magnetic field, which supports the antiferromagnetic coupling nature concluded in the main text. In the meantime, Eq. (E5) shows that $\delta k_{1,YIG}^2$ has the same sign as J , which means that if $J < 0 \text{ mJ/m}^2$, then $\delta k_{1,YIG}^2 < 0$. According to Eq. (C12), under the same external magnetic field, the resonant frequency required by

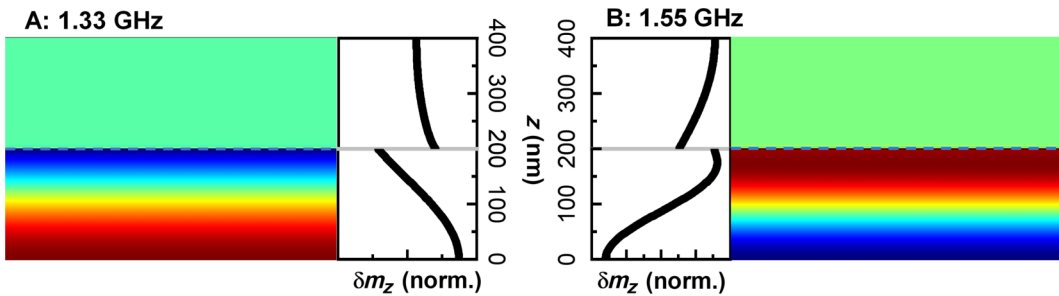


FIG. 10. Two hybrid eigenmodes at 10.5 mT. The δm_z distribution of the normalized intensity is in the z -direction for the two hybrid modes at 1.33 GHz and 1.55 GHz.

the TmIG/YIG sample is smaller than that of YIG/GGG, which is consistent with our results (Fig. 13). We can also roughly estimate the interfacial exchange energy

$$\left(J \approx H_{\text{shift}} \times \frac{M_{s1} + M_{s2}}{2} \times d_1 = -0.0042 \text{ T} \right. \\ \left. \times 133.3 \text{ kA/m} \times 100 \text{ nm} = -0.0598 \text{ mJ/m}^2 \right)$$

by observing the shift in the FMR curve between the TmIG/YIG/GGG heterostructure and the YIG/GGG single layer.

TABLE II. Parameters used when undertaking the micromagnetic simulation for the TmIG (200 nm)/YIG (200 nm) bilayer in Figs. 9 and 10.

Parameters	Symbol	Value
Mesh	N	$20 \times 20 \times 50$
Microwave field	h_{rf}	0.001 T
Interfacial exchange energy	J	-0.0537 mJ/m^2
YIG/TmIG gyromagnetic ratio	$\gamma_{\text{YIG}}/\gamma_{\text{TmIG}}$	28/21.81 GHz/T
YIG/TmIG stiffness constant	$A_{\text{ex,YIG}}/A_{\text{ex,TmIG}}$	3.08/2.67 pJ/m
YIG/TmIG Gilbert damping	$\alpha_{\text{YIG}}/\alpha_{\text{TmIG}}$	$6.66 \times 10^{-4}/1.17 \times 10^{-3}$
Frequency range	$(f_{\text{start}}, \Delta f, f_{\text{end}})$	(1, 0.01, 4) GHz
Magnetic field range	$(H_{\text{start}}, \Delta H, H_{\text{end}})$	(30, 5, 700) Oe

2. Thickness dependence of interfacial exchange energy and coupling strength for the TmIG/YIG samples

a. Interfacial exchange energy

Figs. 14(a)–14(c) show the color map of the spin-wave absorption spectra for the PSSW modes of TmIG

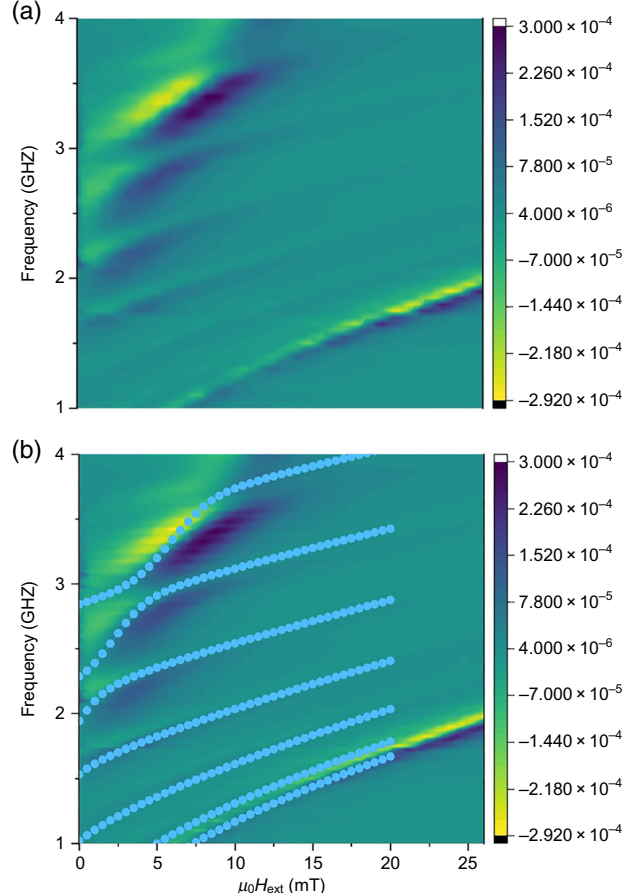


FIG. 11. Magnetic field dependency of resonant peaks for the CoFeB(50 nm)/TmIG (350 nm) heterostructure. (a) Experimentally color-coded spin-wave absorption spectra of the CoFeB (50 nm)/TmIG (350 nm) heterostructure for the first seven resonance modes of TmIG ($n=0-6$) and the uniform mode of CoFeB ($n=0$). (b) Fitting of the ferromagnetic interfacial coupling energy by theoretical calculation.

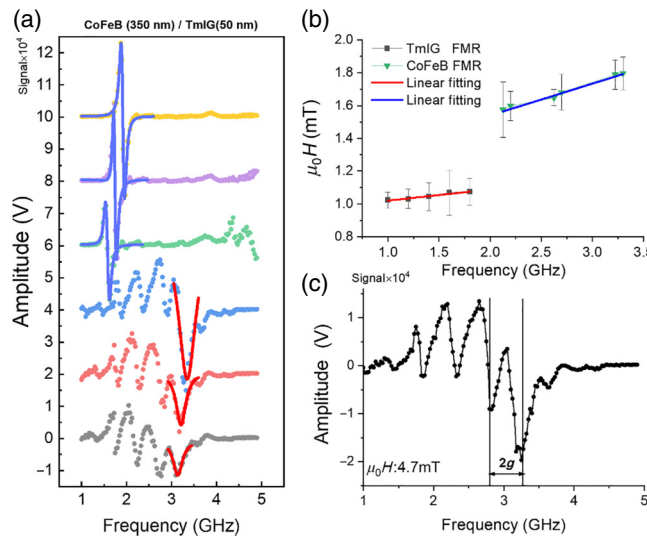


FIG. 12. (a) Dissipation rate, (b) Gilbert damping, and (c) coupling strength of the TmIG (50 nm)/CoFeB (350 nm) heterostructure extracted from the experimental data.

and the uniform mode of YIG measured for the TmIG (100 nm)/YIG(100 nm), TmIG(140 nm)/YIG(140 nm), and TmIG(200 nm)/YIG(200 nm) heterostructures. We fit the experimental data [Figs. 14(e) and 14(f)] through a numerical analysis, as given in Appendix C. The results are summarized in Table I.

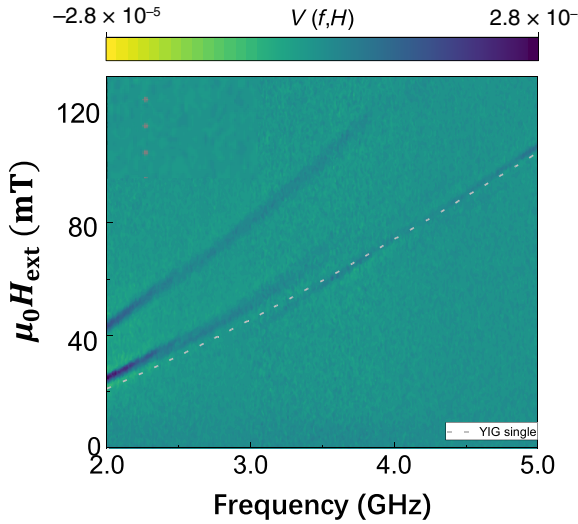


FIG. 13. Spin-wave absorption spectra for TmIG (100 nm)/YIG (100 nm) in comparison with YIG (100 nm)/GGG (gray dashed line). A lower resonant magnetic field $\mu_0 H_{\text{ext}}$, or higher resonant frequency ω_{res} , is observed for YIG (100 nm)/GGG both before and after the avoided crossing. This demonstrates that, for the TmIG/YIG sample, the interfacial exchange field applied on YIG is opposite to the external magnetic field, which supports the antiferromagnetic coupling nature concluded in the main text.

b. Coupling strength g

We can also extract the magnon-magnon coupling strength, which is defined as half of the minimal peak-to-peak frequency spacing in the anticrossing induced by the interfacial exchange energy [37,54]. When the interfacial exchange energy is 0 ($J = 0$ mJ/m²), the hybrid modes are decoupled. The resonant magnetic field (H_{ext}) and resonant frequency (f), where the minimum resonant separation is located, should intersect, meaning that $k_1 = 0$ and $k_2 = n\pi/d_2$. With the existence of the interfacial exchange coupling energy ($J \neq 0$ mJ/m²), we can obtain the perturbative solution. We modify Eq. (C12) to derive an expression of the coupling strength $g(\delta f/2)$ so that

$$2f_{\text{res}}\delta f = \left(\frac{\gamma}{2\pi}\right)^2 \left[2(2\mu_0 H_{\text{res}} + \mu_0 M_s) \frac{2A_{\text{ex}}}{M_s} k \delta k \right. \\ \left. + \left(\frac{2A_{\text{ex}}}{M_s}\right)^2 4k^3 dk \right]. \quad (\text{E1})$$

For Eq. (C23), we can let $(2A_{\text{ex},1}/M_{s,1})k_1 \tan(k_1 d_1)$ be A and $(2A_{\text{ex},2}/M_{s,2})k_2 \tan(k_2 d_2)$ be B . So, Eq. (C23) can be simplified to

$$1 - \frac{2J}{(M_{s,1} + M_{s,2})} \left(\frac{1}{A} + \frac{1}{B}\right) = 0. \quad (\text{E2})$$

We now consider $k_1 = 0 + \delta k_1$, $k_2 = n\pi/d_2 + \delta k_2$, and $|\delta k_1| \ll 1$, $|\delta k_2| \ll 1$ is the perturbation solution corresponding to the minimum resonance separation of the FMR mode of YIG and TmIG PSSW mode (n). Equation (E2) yields a layer 1-dominated and layer 2-dominated resonance. For a layer 1-dominated resonance, we have

$$\frac{2J}{(M_{s,1} + M_{s,2})} \frac{1}{A} \approx 1 \text{ and } \frac{2J}{(M_{s,1} + M_{s,2})} \frac{1}{B} \ll 1, \quad (\text{E3})$$

$$\frac{2J}{(M_{s,1} + M_{s,2})} \approx \frac{2A_{\text{ex},1}}{M_{s,1}} k_1 \tan(k_1 d_1) = \frac{2A_{\text{ex},1}}{M_{s,1}} k_1 \delta k_1 d_1 \\ = \frac{2A_{\text{ex},1}}{M_{s,1}} \delta k_1^2 d_1, \quad (\text{E4})$$

$$\delta k_1^2 = \frac{2J}{(M_{s,1} + M_{s,2})} \frac{M_{s,1}}{2A_{\text{ex},1}} \frac{1}{d_1}. \quad (\text{E5})$$

For $k_1 = \delta k_1$, $(2\mu_0 H + \mu_0 M_s)(2A_{\text{ex}}/M_s)2\delta k_1 \gg (2A_{\text{ex}}/M_s)^2 4\delta k_1^3$ so that

$$\delta f_1 \approx \left(\frac{\gamma_1}{2\pi}\right)^2 \left[2(2\mu_0 H_{\text{res}} + \mu_0 M_{s,1}) \frac{2J}{(M_{s,1} + M_{s,2})} \frac{1}{d_1} \right] \frac{1}{2f_{\text{res}}}. \quad (\text{E6})$$

For a layer 2-dominated resonance, we find

$$\frac{2J}{(M_{s,1} + M_{s,2})} \frac{1}{B} \approx 1 \text{ and } \frac{2J}{(M_{s,1} + M_{s,2})} \frac{1}{A} \ll 1, \quad (\text{E7})$$

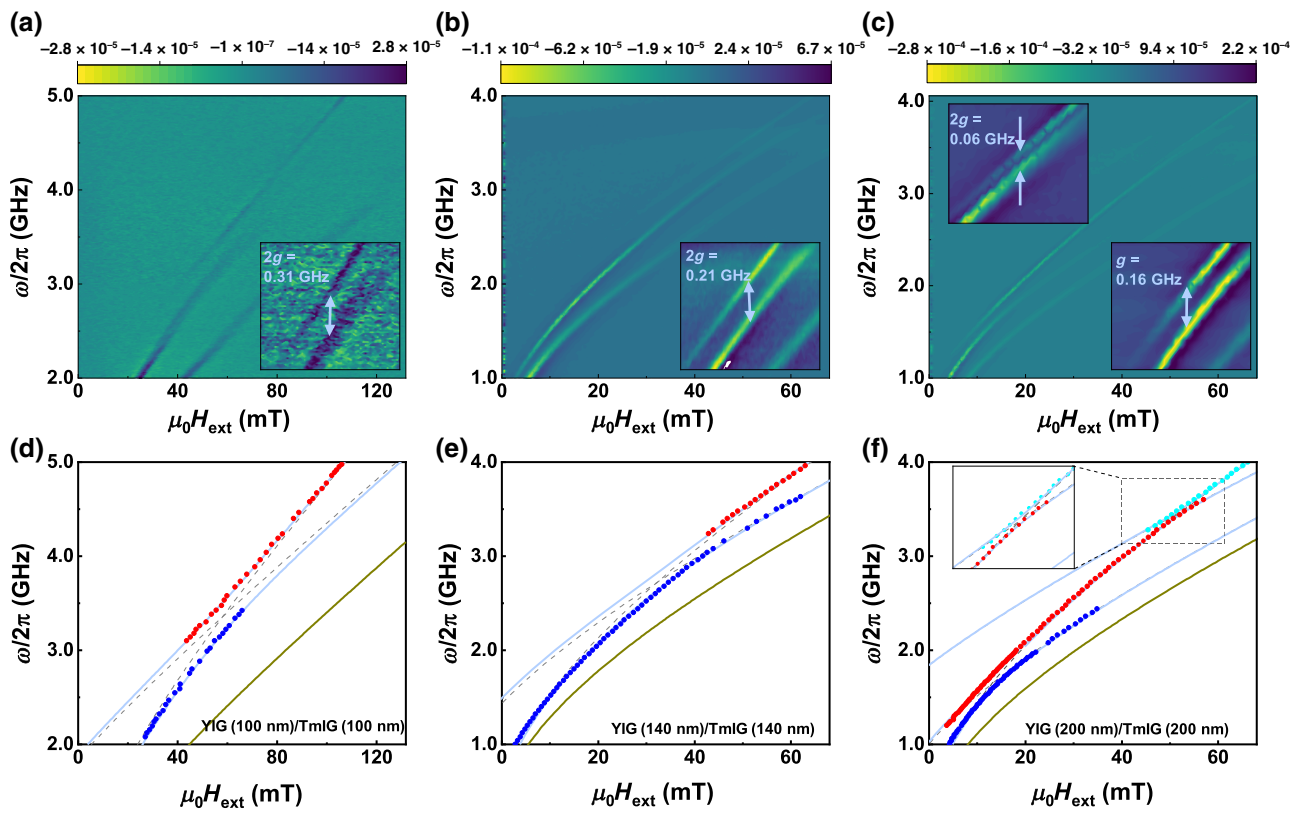


FIG. 14. Magnetic insulator heterostructure thickness dependence of the strong magnon-magnon coupling. Experimentally color-coded spin-wave absorption spectra for (a) YIG (100 nm)/TmIG(100 nm), (b) YIG (140 nm)/TmIG(140 nm), and (c) YIG (200 nm)/TmIG(200 nm). Insets show magnification at each anticrossing region. Resonant absorption peaks of the two hybrid modes as a function of the external magnetic field with a (e) YIG (100 nm)/TmIG(100 nm), (f) YIG (140 nm)/TmIG(140 nm), and (g) YIG (200 nm)/TmIG(200 nm) bilayer. Solid curves represent the numerical theory method fits as hybrid modes using the method of Appendix C. Data points are extracted from experimental data by fitting the line shapes to two independent derivative Lorentzian functions in (a)–(c). The increase of the effective magnetization in YIG and TmIG and the stiffening of YIG and TmIG resonance frequency are due to the increase of different magnetic insulator thicknesses.

$$\delta k_2 = \frac{2J}{(M_{s,1} + M_{s,2})} \frac{M_{s,2}}{2A_{\text{ex},2}} \frac{1}{n\pi/d_2} \frac{1}{d_2}. \quad (\text{E8})$$

For

$$k_2 = \frac{n\pi}{d_2} + \delta k_2, (2\mu_0 H + \mu_0 M_s) \sim 10^{-1}, \frac{2A_{\text{ex}}}{M_s} \sim 10^{-18},$$

$$\text{and } k_2 \sim \frac{n\pi}{d_2} \sim 10^7,$$

we can obtain

$$(2\mu_0 H + \mu_0 M_s) \frac{2A_{\text{ex}}}{M_s} 2k_2 \sim 10^{-12}$$

$$\gg \left(\frac{2A_{\text{ex}}}{M_s} \right)^2 4k^3 \sim 10^{-15},$$

$$\delta f_2 \approx \left(\frac{\gamma_2}{2\pi} \right)^2 \left[2(2\mu_0 H_{\text{res}} + \mu_0 M_{s,2}) \frac{2J}{(M_{s,1} + M_{s,2})} \frac{1}{d_2} \right] \frac{1}{2f_{\text{res}}}, \quad (\text{E9})$$

$$\delta f^2 = \left(\frac{\gamma_1}{2\pi} \right)^2 \left(\frac{\gamma_2}{2\pi} \right)^2 \left(\frac{2J}{(M_{s,1} + M_{s,2})} \right)^2 \times \frac{[(2\mu_0 H_{\text{res}} + \mu_0 M_{s,1})(2\mu_0 H_{\text{res}} + \mu_0 M_{s,2})]}{f_{\text{res}}^2} \frac{1}{d_1 d_2}, \quad (\text{E10})$$

$$g = \frac{\delta f}{2} = \frac{\gamma_1}{2\pi} \frac{\gamma_2}{2\pi} \frac{|J|}{(M_{s,1} + M_{s,2})} \times \frac{\sqrt{(2\mu_0 H_{\text{res}} + \mu_0 M_{s,1})(2\mu_0 H_{\text{res}} + \mu_0 M_{s,2})}}{f_{\text{res}}} \frac{1}{\sqrt{d_1 d_2}}, \quad (\text{E11})$$

where g is the coupling strength, H_{res} and f_{res} are the resonant magnetic field and frequency at the minimum resonance separation, respectively, and d_1 and d_2 are the thicknesses of the YIG layer (the FMR mode) and TmIG layer (the PSSW mode), respectively. The g value extracted from the experiments [Figs. 15(a)–15(c)] and the calculations from Eq. (E11) are shown in Fig. 4(c).

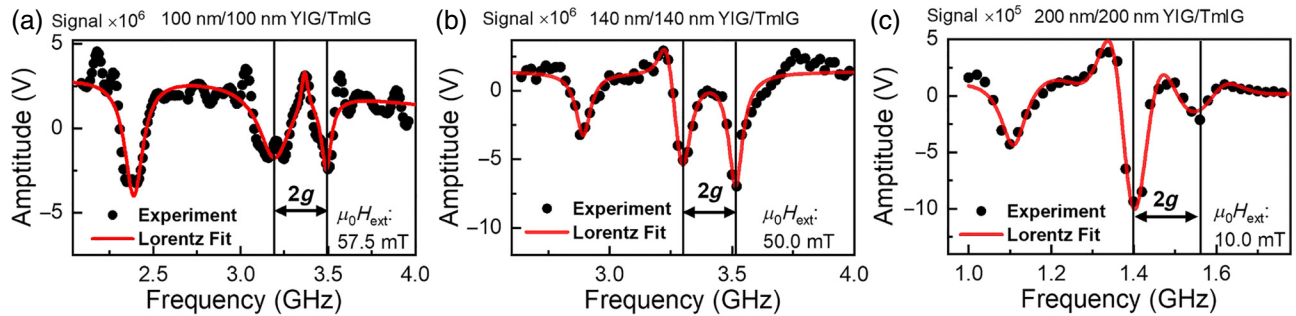


FIG. 15. Magnetic insulator heterostructure thickness dependence of the coupling strength. Experimental spin-wave spectra at the minimum resonance separation with frequency for (a) TmIG (100 nm)/YIG (100 nm), (b) TmIG (140 nm)/YIG (140 nm), and (c) TmIG (200 nm)/YIG (200 nm). Here, the red line is fitted by the Lorentz peak function to coupling strength.

APPENDIX F: THE EXCITATION OF GILBERT DAMPING, DISSIPATION RATE, AND COOPERATIVITY FROM FMR MEASUREMENTS

1. Gilbert damping α

High coupling strength g and extremely low Gilbert damping α are key factors to realize long-distance information transmission that is free of Joule heating. Gilbert damping refers to an intrinsic feature of magnetic substances, which dictates the speed at which angular momentum is transferred to the crystal lattice, which is the key parameter that determines the spin-wave relaxation [55,56]. To demonstrate the superiority of the low-damping MI/MI bilayer system of this work, we focus on the linewidth variations with the frequency of the YIG/TmIG heterostructure samples. The linewidth versus frequency experiment data with error bars for different thicknesses were extracted by fitting Lorentz equations in Fig. 16. In the strong coupling region, we can clearly observe that the linewidth value of the pink circle is significantly higher than that of the light blue circle, which

suggests a coherent dampinglike torque that acts along or against the intrinsic damping torque depending on the phase difference of the coupled dynamics of YIG and TmIG [35]. Distant from the strong coupling region, we use $\Delta H = \Delta H_0 + (4\pi\alpha/\gamma)f$ for the linear characterization; the result is indicated by the dashed line in Fig. 16. The fitting effective damping constants are summarized in Table I.

2. Dissipation rate

We extract the dissipation rate (half-width at half-maximum) from frequency scans at different fields when they are distant from the strong coupling region (Fig. 17). We fit the FMR mode of YIG and TmIG in Fig. 17 using a Lorentz peak to obtain the dissipation rate.

3. Cooperativity C

Strong coupling implies coherent dynamics between the magnon. In our case, for all the samples, $g > \kappa_1$ and $g > \kappa_2$ mean that strong coupling is formed [37,57]. Through

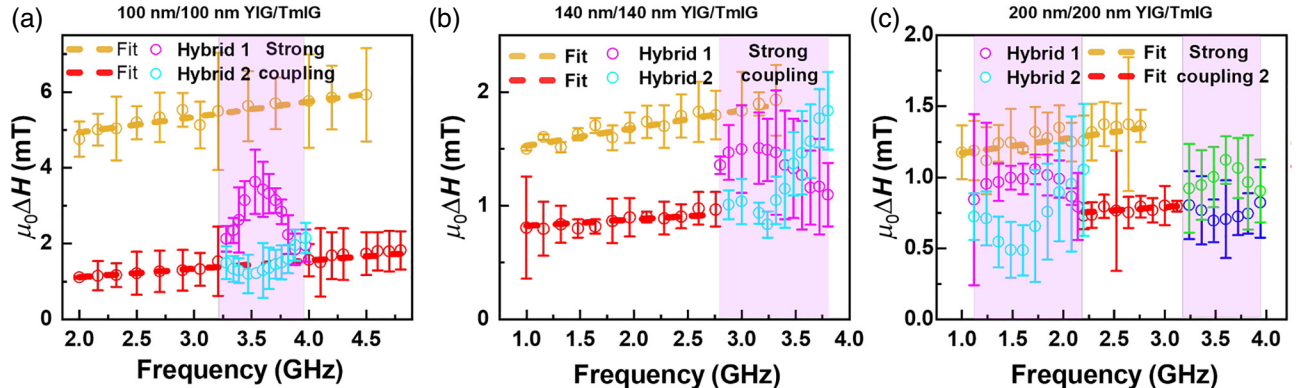


FIG. 16. Thickness dependence of Gilbert damping. Experimental linewidth as a function of frequency for (a) TmIG (100 nm)/YIG (100 nm), (b) TmIG (140 nm)/YIG (140 nm), and (c) TmIG (200 nm)/YIG (200 nm). Circular points with the error bars represent the linewidths extracted from experimental data by fitting the line shapes to three independent derivative Lorentzian functions from (a)–(c). Dashed lines are linear fits distant from the strong coupling region by using Eq. (4). The fitting effective damping constants are summarized in Table II.

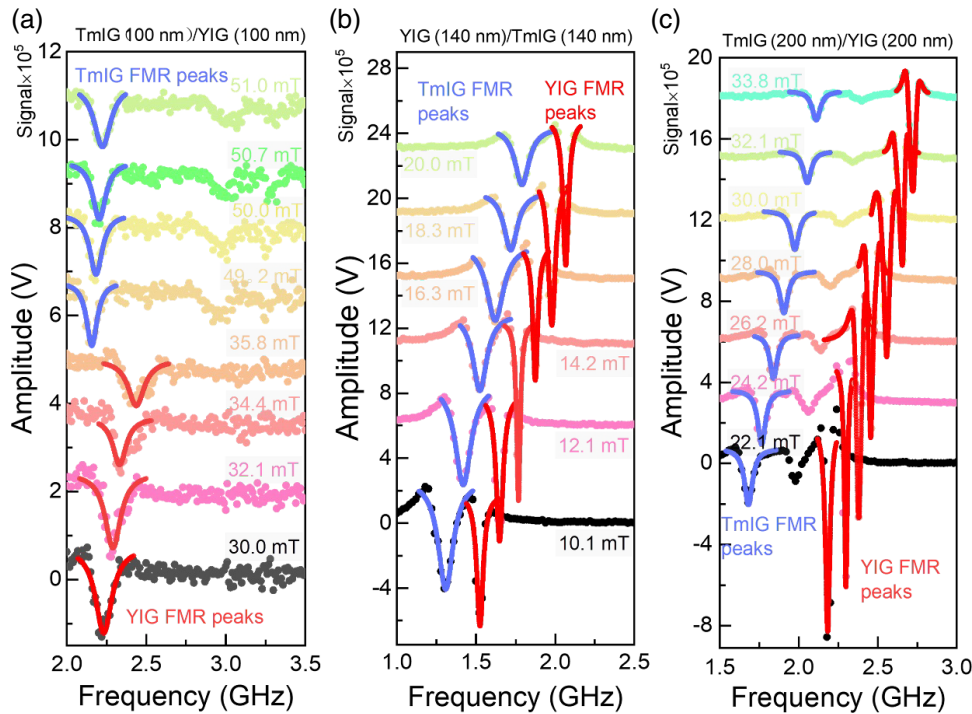


FIG. 17. Thickness dependence of the dissipation rate. Amplitude as a function of frequency for (a) TmIG (100 nm)/YIG (100 nm), (b) TmIG (140 nm)/YIG (140 nm), and (c) TmIG (200 nm)/YIG (200 nm). Frequency sweep curves distant from the coupling region. The dissipation rate is obtained by fitting a Lorentzian peak function. The red solid line represents YIG FMR, and the blue solid line represents TmIG FMR.

Lorentz peak fitting, we found that the dissipation rate decreases as the thickness increases, which is consistent with the damping trend we have calculated. Due to the magnetic insulator heterostructure, the dissipation rates in the TmIG/YIG bilayers are particularly low compared with those in ferromagnetic metal-based heterostructures, allowing us to achieve the largest cooperativity $C = (g/\kappa_1)(g/\kappa_2) = 24.5$ in the TmIG(200 nm)/YIG(200 nm) case. The results are summarized in Table II. As the thickness increases, the cooperativity significantly increases, mainly because the decrease rate of the dissipation rates is greater than that of the coupling strength. The cooperativity is summarized in Table I.

APPENDIX G: TOPOLOGICAL NONTRIVIAL MAGNONIC BAND STRUCTURE IN ALL-MAGNETIC INSULATOR-BASED MULTILAYERS

As a recent theory [39] predicted, antiparallelly aligned multilayers can potentially host topological nontrivial magnonic band structures. The magnetic multilayers are shown in Fig. 18, where the neighboring layers possess antiferromagnetic interfacial exchange. Due to the essentially in-plane propagating chiral dipole interaction and interfacial exchange interaction, the bulk energy band

of the multilayer films generates nonzero Chern integers and ultralocalized magnonic surface states carrying chiral spin currents. Here, we show our recent progress in the theoretical understanding of all-magnetic insulator heterostructure-based topological magnonic insulators. Compared with achieving high-quality interfaces and all-magnetic insulator-based multilayer systems through pulsed laser deposition (PLD) technology, growing high-quality YIG on polycrystalline Py is challenging.

To perform the calculations, we use the experimentally extracted parameters from our YIG/TmIG multilayers. The requirement to achieve a topological nontrivial state is to have

$$\left(\frac{A_{\text{ex},\text{YIG}}\gamma_{\text{YIG}}}{M_{s,\text{YIG}}} - \frac{A_{\text{ex},\text{TmIG}}\gamma_{\text{TmIG}}}{M_{s,\text{TmIG}}} \right) \times \left[\gamma_{\text{YIG}} \left(\frac{2|J|}{\mu_0 M_{s,\text{YIG}} d_{\text{YIG}}} - H \right) - \gamma_{\text{TmIG}} \left(\frac{2|J|}{\mu_0 M_{s,\text{TmIG}} d_{\text{TmIG}}} + H \right) \right] < 0,$$

where the obtained critical field $H_c = 4.55 \times 10^3$ A/m. For comparison, we plot the magnon band structures [frequency (f') and wave vector (k_x)] based on all-magnetic insulators YIG/TmIG [Figs. 18(a) and 18(b)] and YIG/Py [Figs. 18(c) and 18(d)] based system with

$N=10$ cells, respectively. We can see a clear distinction between topologically nontrivial and trivial states for the two systems, which can provide potentially enormous nonreciprocity and be tuned by the external field. We also see that the nontrivial state of the multilayer films based on YIG/Py needs to be realized at $(k, f) \approx (-1.5 \times 10^8 \text{ m}^{-1}, 51 \text{ GHz})$. However, except for the challenges of microwave measurement, most of the experimental work on magnon-based computing and signal transmission has been conducted in the k range $10^6\text{--}10^8 \text{ m}^{-1}$ [58,59]. Conversely, all-magnetic insulator-based multilayers are not subject to these limitations,

which can be achieved with reasonable excitation frequency and corresponding k values.

In the general case, magnons can propagate within the entire xy -plane in each individual layer. Magnons propagating in neighboring layers are coupled with each other through Zeeman interactions, interfacial exchange interactions, and long-range dipolar interactions.

A. The interlayer dipolar energy between a pair of moments \mathbf{m}_1 (located at \mathbf{r}) and \mathbf{m}_2 (located at \mathbf{r}') is given by

$$\delta E_d = \mathbf{m}_2^T \mathbf{F} \mathbf{m}_1 = -\frac{\mu_0 M_{s1} M_{s2}}{4\pi} \frac{3(\mathbf{m}_1 \cdot \mathbf{R})(\mathbf{m}_2 \cdot \mathbf{R}) - (\mathbf{m}_1 \cdot \mathbf{m}_2)R^2}{R^5}, \quad \mathbf{R} = \mathbf{r} - \mathbf{r}', \quad (\text{G1})$$

$$E_d = \iint \mathbf{m}_2^T(\mathbf{r}') \mathbf{F}(\mathbf{r} - \mathbf{r}') \mathbf{m}_1(\mathbf{r}) d^3r d^3r'. \quad (\text{G2})$$

Each layer interlayer dipolar effective field ($\tilde{h}_j^{d\dagger}(k)$) of the magnons in k -space after Fourier transformation of E_d is given by the following:

$$\begin{bmatrix} \tilde{h}_{1,x}^{d\dagger}(k_x) \\ \tilde{h}_{1,z}^{d\dagger}(k_x) \end{bmatrix} = M_{s,2} d_2 \frac{k_x d_1 [1 - (-1)^m e^{-k_x d_1}]}{[(k_x d_1)^2 + (m\pi)^2]} \begin{bmatrix} |k_x| \sin \theta_1 \sin \theta_2 & ik_x \sin \theta_1 \\ ik_x \sin \theta_2 & -|k_x| \end{bmatrix} \begin{bmatrix} \tilde{m}_{1,x}(k_x) \cos(m\pi z/d_1) \\ \tilde{m}_{1,z}(k_x) \cos(m\pi z/d_1) \end{bmatrix}, -d_1 < z < 0, \quad (\text{G3})$$

$$\begin{bmatrix} \tilde{h}_{2,x}^{d\dagger}(k_x) \\ \tilde{h}_{2,z}^{d\dagger}(k_x) \end{bmatrix} = M_{s,1} d_1 \frac{k_x d_2 [1 - (-1)^n e^{-k_x d_2}]}{[(k_x d_2)^2 + (n\pi)^2]} \begin{bmatrix} |k_x| \sin \theta_1 \sin \theta_2 & -ik_x \sin \theta_2 \\ -ik_x \sin \theta_1 & -|k_x| \end{bmatrix} \begin{bmatrix} \tilde{m}_{2,x}(k_x) \cos(n\pi z/d_2) \\ \tilde{m}_{2,z}(k_x) \cos(n\pi z/d_2) \end{bmatrix}, 0 < z < d_2, \quad (\text{G4})$$

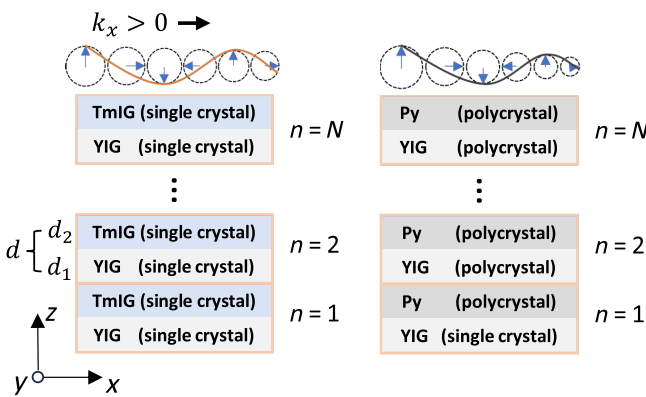


FIG. 18. Schematic of the antiparallel-aligned all-magnetic-insulator YIG/TmIG-based multilayers and YIG/Py-based multilayers. The process of achieving high-quality yttrium iron garnet (YIG) on polycrystalline Py compared with the single-crystal all-magnetic insulator-based multilayer systems using pulsed laser deposition (PLD) technology. The low Gilbert damping of YIG/TmIG allows for reduced dissipation in spin-wave propagation.

where m and n are the standing wave modes in the z -direction of the magnetic layers.

B. The intralayer dipolar interaction can be simplified from a condition

$$\begin{bmatrix} \tilde{h}_{1,x}^{d0}(k_x) \\ \tilde{h}_{1,z}^{d0}(k_x) \end{bmatrix} = M_{s,1} \begin{bmatrix} (1 - N_1) & 0 \\ 0 & N_1 \end{bmatrix} \times \begin{bmatrix} \tilde{m}_{1,x}(k_x) \cos(m\pi z/d_1) \\ \tilde{m}_{1,z}(k_x) \cos(m\pi z/d_1) \end{bmatrix}, N_1 = \frac{k_x d_1 [1 - (-1)^m e^{-k_x d_1}]}{[(k_x d_1)^2 + (m\pi)^2]}, \quad (\text{G5})$$

$$\begin{bmatrix} \tilde{h}_{2,x}^{d0}(k_x) \\ \tilde{h}_{2,z}^{d0}(k_x) \end{bmatrix} = M_{s,2} \begin{bmatrix} (1 - N_2) & 0 \\ 0 & N_2 \end{bmatrix}$$

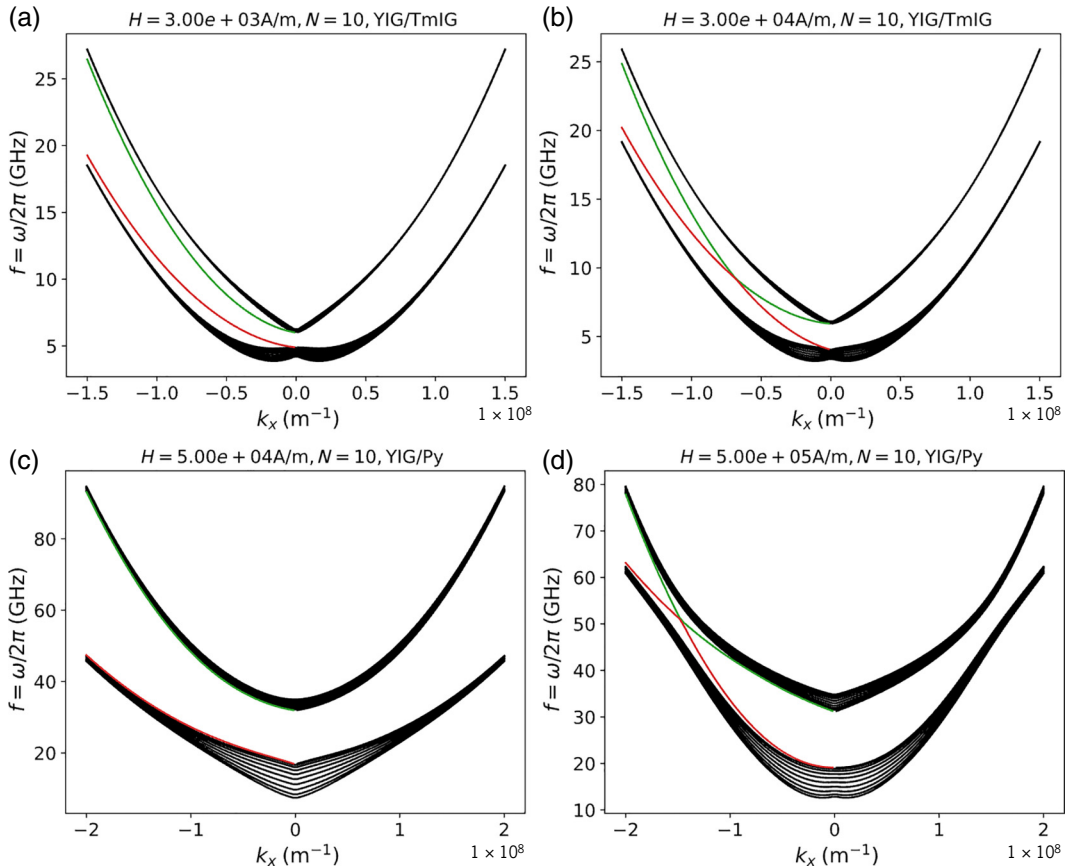


FIG. 19. Magnon band structures for the all-magnetic insulator with a YIG/TmIG-based system with $N = 10$ cells, which correspond to the (a) trivial case with $H = 3 \times 10^3 \text{ A/m}$ and (b) topological nontrivial state with $H = 3 \times 10^4 \text{ A/m}$, and with a YIG/Py-based system with $N = 10$ cells, which correspond to the (c) trivial case ($H = 5 \times 10^4 \text{ A/m}$) and (d) topological nontrivial state ($H = 5 \times 10^5 \text{ A/m}$).

$$\begin{aligned} & \times \begin{bmatrix} \tilde{m}_{2,x}(k_x) \cos(n\pi z/d_1) \\ \tilde{m}_{2,z}(k_x) \cos(n\pi z/d_1) \end{bmatrix}, N_2 \\ &= \frac{k_y d_2 [1 - (-1)^n e^{-k_x d_2}]}{[(k_x d_2)^2 + (n\pi)^2]}. \end{aligned} \quad (\text{G6})$$

The intralayer exchange field is given by

$$\tilde{h}_{j,x(z)}^{\text{ex0}} = -\frac{2A_j^{\text{ex}} k_j^2}{\mu_0 M_{s,j}} \tilde{m}_{j,x(z)}, j = 1, 2. \quad (\text{G7})$$

The static interfacial exchange field is written as

$$H_j^{\text{ex}} = 2J/\mu_0 M_{s,j} d_j, j = 1, 2. \quad (\text{G8})$$

The dynamic interfacial exchange field is

$$\begin{bmatrix} \tilde{h}_{jx}^{\text{ex}}(\mathbf{k}_\parallel) \\ \tilde{h}_{jz}^{\text{ex}}(\mathbf{k}_\parallel) \end{bmatrix} = H_j^{\text{ex}} \begin{bmatrix} 1/2 & 0 \\ 0 & -1/2 \end{bmatrix} \begin{bmatrix} \tilde{m}_{vx}(\mathbf{k}_\parallel) \\ \tilde{m}_{vz}(\mathbf{k}_\parallel) \end{bmatrix}. \quad (\text{G9})$$

We obtain the full Hamiltonian by integrating all the interactions so that

$$\omega \begin{pmatrix} \tilde{m}_{1+} \\ \tilde{m}_{2+} \\ \tilde{m}_{1-} \\ \tilde{m}_{2-} \end{pmatrix} = \begin{pmatrix} \omega'_1 & \Delta'_{1+} & \delta_1 & \delta'_1 \\ \Delta'_{2+} & \omega'_2 & \delta'_2 & \delta_2 \\ -\delta_1 & -\delta'_1 & -\omega'_1 & \Delta'_{1-} \\ -\delta'_2 & -\delta_2 & \Delta'_{2-} & -\omega'_2 \end{pmatrix} \begin{pmatrix} \tilde{m}_{1+} \\ \tilde{m}_{2+} \\ \tilde{m}_{1-} \\ \tilde{m}_{2-} \end{pmatrix}, \quad (\text{G10})$$

where the intrinsic eigenstate $\tilde{m}_{j\pm} = 1/\sqrt{2} (\tilde{m}_{jx} \pm i\tilde{m}_{jz})$ is a right- and left-handed circularly polarized magnon mode, which corresponds to the positive and negative eigenfrequency, representing a particle and hole, respectively. We also find that

$$\omega'_j = \frac{2A_j^{\text{ex}}\gamma_j}{M_{s,j}}k_x^2 + \gamma_j\mu_0\sqrt{(2J/\mu_0M_{s,j}d_j + H_{\text{ext}} + M_{s,j})(2J/\mu_0M_{s,j}d_j + H_{\text{ext}})} + \frac{\gamma_j\mu_0M_{s,j}}{2}, \quad (\text{G11})$$

$$\Delta'_{j\pm} = \frac{1}{2}\gamma_j\mu_0f'_j[\pm(2k_x) + 2k_x], \quad (\text{G12})$$

$$\delta_j = \frac{\gamma_j\mu_0M_{s,j}}{2}, \quad (\text{G13})$$

$$\delta'_j = \frac{\gamma_j\mu_0}{2}\frac{2J}{\mu_0M_{s,j}d_j}. \quad (\text{G14})$$

After utilizing the Holstein-Primakoff transformation on \tilde{m}_{j+} and \tilde{m}_{j-} , we can either derive the bulk Hamiltonian with periodic boundary conditions along the z -direction or solve for the explicit band structure with open boundary conditions along the z -direction. In the case of n cells, the bulk Hamiltonian can be regarded as a tight-binding Hamiltonian in the z -direction, and then the Su-Schrieffer-Heeger (SSH) model is used to solve it, as shown in Fig. 19. The all-insulator multilayer system facilitates the realization of the topological magnonic surface states and the low dissipation spin current transport in a tunable manner.

-
- [1] A. V. Chumak, V. I. I. Vasyuchka, A. A. A. Serga, and B. Hillebrands, Magnon spintronics, *Nat. Phys.* **11**, 453 (2015).
- [2] A. Khitun, M. Bao, and K. L. Wang, Magnonic logic circuits, *J. Phys. D: Appl. Phys.* **43**, 264005 (2010).
- [3] V. Kruglyak, O. Demokritov, and D. Grundler, Preface: Magnonics, *J. Phys. D: Appl. Phys.* **43**, 29 (2010).
- [4] P. Pirro, V. I. Vasyuchka, A. A. Serga, and B. Hillebrands, Advances in coherent magnonics, *Nat. Rev. Mater.* **6**, 1114 (2021).
- [5] H. Y. Yuan, Y. Cao, A. Kamra, R. A. Duine, and P. Yan, Quantum magnonics: When magnon spintronics meets quantum information science, *Phys. Rep.* **965**, 1 (2022).
- [6] L. J. Cornelissen, J. Liu, R. A. Duine, J. Ben Youssef, and B. J. Van Wees, Long-distance transport of magnon spin information in a magnetic insulator at room temperature, *Nat. Phys.* **11**, 1022 (2015).
- [7] Y. Kajiwara, K. Harii, S. Takahashi, J. Ohe, K. Uchida, M. Mizuguchi, H. Umezawa, H. Kawai, K. Ando, K. Takanashi, S. Maekawa, and E. Saitoh, Transmission of electrical signals by spin-wave interconversion in a magnetic insulator, *Nature* **464**, 262 (2010).
- [8] K. Uchida, J. Xiao, H. Adachi, J. Ohe, S. Takahashi, J. Ieda, T. Ota, Y. Kajiwara, H. Umezawa, H. Kawai, G. E. W. Bauer, S. Maekawa, and E. Saitoh, Spin Seebeck insulator, *Nat. Mater.* **9**, 894 (2010).
- [9] C. O. Avci, A. Quindeau, C.-F. F. Pai, M. Mann, L. Caretta, A. S. Tang, M. C. Onbasli, C. A. Ross, and G. S. D. Beach, Current-induced switching in a magnetic insulator, *Nat. Mater.* **16**, 309 (2017).
- [10] Q. Shao, *et al.*, Role of dimensional crossover on spin-orbit torque efficiency in magnetic insulator thin films, *Nat. Commun.* **9**, 3612 (2018).
- [11] Q. Shao, Y. Liu, G. Yu, S. K. Kim, X. Che, C. Tang, Q. L. He, Y. Tserkovnyak, J. Shi, and K. L. Wang, Topological Hall effect at above room temperature in heterostructures composed of a magnetic insulator and a heavy metal, *Nat. Electron.* **2**, 182 (2019).
- [12] Saül Vélez, Sandra Ruiz-Gómez, Jakob Schaab, Elzbieta Gradauskaitė, Martin S. Wörnle, Pol Welter, Benjamin J. Jacot, Christian L. Degen, Morgan Trassin, Manfred Fiebig, and Pietro Gambardella, Current-driven dynamics and ratchet effect of skyrmion bubbles in a ferrimagnetic insulator, *Nat. Nanotechnol.* **17**, 834 (2022).
- [13] S. O. Demokritov, V. E. Demidov, O. Dzyapko, G. A. Melkov, A. A. Serga, B. Hillebrands, and A. N. Slavin, Bose-Einstein condensation of quasi-equilibrium magnons at room temperature under pumping, *Nature* **443**, 430 (2006).
- [14] T. Giamarchi, C. Rüegg, and O. Tchernyshyov, Bose-Einstein condensation in magnetic insulators, *Nat. Phys.* **4**, 198 (2008).
- [15] Y. Tserkovnyak, S. A. Bender, R. A. Duine, and B. Flebus, Bose-Einstein condensation of magnons pumped by the bulk spin Seebeck effect, *Phys. Rev. B* **93**, 1 (2016).
- [16] S. Takei and Y. Tserkovnyak, Superfluid spin transport through easy-plane ferromagnetic insulators, *Phys. Rev. Lett.* **112**, 227201 (2014).
- [17] B. Flebus, S. A. Bender, Y. Tserkovnyak, and R. A. Duine, Two-fluid theory for spin superfluidity in magnetic insulators, *Phys. Rev. Lett.* **116**, 1 (2016).
- [18] A. Qaiumzadeh, H. Skarsvåg, C. Holmqvist, and A. Brataas, Spin superfluidity in biaxial antiferromagnetic insulators, *Phys. Rev. Lett.* **118**, 1 (2017).
- [19] R. Chisnell, J. S. Helton, D. E. Freedman, D. K. Singh, R. I. Bewley, D. G. Nocera, and Y. S. Lee, Topological magnon bands in a kagome lattice ferromagnet, *Phys. Rev. Lett.* **115**, 147201 (2015).
- [20] R. A. Duine, K.-J. Lee, S. S. P. Parkin, and M. D. Stiles, Synthetic antiferromagnetic spintronics, *Nat. Phys.* **14**, 217 (2018).
- [21] E. Deeson, *Springer Tracts in Modern Physics* (Springer Berlin, Heidelberg, 1972), Vol. 58, Vol. 23.
- [22] Y. Huai, Spin-transfer torque MRAM (STT-MRAM): Challenges and prospects, *AAPPS Bull.* **18**, 33 (2008).
- [23] Juan M. Gomez-Perez, Saül Vélez, Lauren McKenzie-Sell, Mario Amado, Javier Herrero-Martín, Josu López-López, S. Blanco-Canosa, Luis E. Hueso, Andrey Chuvalin, Jason W. A. Robinson, and Félix Casanova, Synthetic antiferromagnetic coupling between ultrathin insulating garnets, *Phys. Rev. Appl.* **10**, 044046 (2018).
- [24] S. Becker, Z. Ren, F. Fuhrmann, A. Ross, S. Lord, S. Ding, R. Wu, J. Yang, J. Miao, M. Kläui, and G. Jakob, Magnetic

- coupling in $\text{Y}_3\text{Fe}_5\text{O}_{12}/\text{Gd}_3\text{Fe}_5\text{O}_{12}$ heterostructures, *Phys. Rev. Appl.* **16**, 014047 (2021).
- [25] R. Kumar, S. N. Sarangi, D. Samal, and Z. Hossain, Positive exchange bias and inverted hysteresis loop in $\text{Y}_3\text{Fe}_5\text{O}_{12}/\text{Gd}_3\text{Ga}_5\text{O}_{12}$, *Phys. Rev. B* **103**, 064421 (2021).
- [26] J. M. Liang, X. W. Zhao, S. M. Ng, H. F. Wong, Y. K. Liu, C. L. Mak, and C. W. Leung, Observation of interfacial anti-ferromagnetic coupling between ferrimagnetic garnet thin films, *IEEE Trans. Magn.* **58**, 1 (2022).
- [27] Patrick Quarterman, Yabin Fan, Zhijie Chen, Christopher J. Jensen, Rajesh V. Chopdekar, Dustin A. Gilbert, Megan E. Holtz, Mark D. Stiles, Julie A. Borchers, Kai Liu, Luqiao Liu, and Alexander J. Grutter, Probing antiferromagnetic coupling in magnetic insulator/metal heterostructures, *Phys. Rev. Mater.* **6**, 094418 (2022).
- [28] H. Wu, L. Huang, C. Fang, B. S. Yang, C. H. Wan, G. Q. Yu, J. F. Feng, H. X. Wei, and X. F. Han, Magnon valve effect between two magnetic insulators, *Phys. Rev. Lett.* **120**, 097205 (2018).
- [29] Joel Cramer, Felix Fuhrmann, Ulrike Ritzmann, Vanessa Gall, Tomohiko Niizeki, Rafael Ramos, Zhiyong Qiu, Dazhi Hou, Takashi Kikkawa, Jairo Sinova, Ulrich Nowak, Eiji Saitoh, and Mathias Kläui, Magnon detection using a ferroic collinear multilayer spin valve, *Nat. Commun.* **9**, 1089 (2018).
- [30] C. Y. Guo, C. H. Wan, X. Wang, C. Fang, P. Tang, W. J. Kong, M. K. Zhao, L. N. Jiang, B. S. Tao, G. Q. Yu, and X. F. Han, Magnon valves based on YIG/NiO/YIG all-insulating magnon junctions, *Phys. Rev. B* **98**, 134426 (2018).
- [31] J. Han, Y. Fan, B. C. McGoldrick, J. Finley, J. T. Hou, P. Zhang, and L. Liu, Nonreciprocal transmission of incoherent magnons with asymmetric diffusion length, *Nano Lett.* **21**, 7037 (2021).
- [32] Y. Fan, P. Quarterman, J. Finley, J. Han, P. Zhang, J. T. Hou, M. D. Stiles, A. J. Grutter, and L. Liu, Manipulation of coupling and magnon transport in magnetic metal-insulator hybrid structures, *Phys. Rev. Appl.* **13**, 061002 (2020).
- [33] H. Qin, R. B. Holländer, L. Flajšman, F. Hermann, R. Dreyer, G. Woltersdorf, and S. van Dijken, Nanoscale magnonic Fabry-Pérot resonator for low-loss spin-wave manipulation, *Nat. Commun.* **12**, 2293 (2021).
- [34] H. Qin, G. J. Both, S. J. Hämäläinen, L. Yao, and S. van Dijken, Low-loss YIG-based magnonic crystals with large tunable bandgaps, *Nat. Commun.* **9**, 1 (2018).
- [35] Yi Li, Wei Cao, Vivek P. Amin, Zhizhi Zhang, Jonathan Gibbons, Joseph Sklenar, John Pearson, Paul M. Haney, Mark D. Stiles, William E. Bailey, Valentine Novosad, Axel Hoffmann, and Wei Zhang, Coherent spin pumping in a strongly coupled magnon-magnon hybrid system, *Phys. Rev. Lett.* **124**, 117202 (2020).
- [36] Stefan Klingler, Vivek Amin, Stephan Geprägs, Kathrin Ganzhorn, Hannes Maier-Flaig, Matthias Althammer, Hans Huebl, Rudolf Gross, Robert D. McMichael, Mark D. Stiles, Sebastian T. B. Goennenwein, and Mathias Weiler, Spin-torque excitation of perpendicular standing spin waves in coupled YIG/Co heterostructures, *Phys. Rev. Lett.* **120**, 127201 (2018).
- [37] J. Chen, C. Liu, T. Liu, Y. Xiao, K. Xia, G. E. W. Bauer, M. Wu, and H. Yu, Strong interlayer magnon-magnon coupling in magnetic metal-insulator hybrid nanostructures, *Phys. Rev. Lett.* **120**, 217202 (2018).
- [38] H. Qin, S. J. Hämäläinen, and S. van Dijken, Exchange-torque-induced excitation of perpendicular standing spin waves in nanometer-thick YIG films, *Sci. Rep.* **8**, 5755 (2018).
- [39] Z. Hu, L. Fu, and L. Liu, Tunable magnonic Chern bands and chiral spin currents in magnetic multilayers, *Phys. Rev. Lett.* **128**, 217201 (2022).
- [40] T. Yu, J. Zou, B. Zeng, J. W. Rao, and K. Xia, Non-Hermitian topological magnonics, *Phys. Rep.* **1062**, 1 (2024).
- [41] J. Nogués and I. K. Schuller, Exchange bias, *J. Magn. Magn. Mater.* **192**, 203 (1999).
- [42] B. Zhang, C. Bin Wu, and W. Kuch, Tailoring interlayer coupling and coercivity in Co/Mn/Co trilayers by controlling the interface roughness, *J. Appl. Phys.* **115**, 233915 (2014).
- [43] K. Tivakornasithorn, T. Yoo, H. Lee, S. Choi, S. Lee, X. Liu, M. Dobrowolska, and J. K. Furdyna, Spacer-thickness dependence of interlayer exchange coupling in GaMnAs/InGaAs/GaMnAs trilayers grown on ZnCdSe buffers, *Solid State Commun.* **253**, 37 (2017).
- [44] R. R. Gareev, V. Zbarsky, J. Landers, I. Soldatov, R. Schäfer, M. Münzenberg, H. Wende, and P. Grünberg, The role of weak interlayer coupling in the spin-reorientation of perpendicular ultrathin Co-Fe-B/MgO-based heterostructures, *Appl. Phys. Lett.* **106**, 132408 (2015).
- [45] Jerad Inman, Yuzan Xiong, Rao Bidhanapally, Steven Louis, Vasyl Tyberkevych, Hongwei Qu, Joseph Sklenar, Valentine Novosad, Yi Li, Xufeng Zhang, and Wei Zhang, Hybrid magnonics for short-wavelength spin waves facilitated by a magnetic heterostructure, *Phys. Rev. Appl.* **17**, 1 (2022).
- [46] S. Crossley, A. Quindeau, A. G. Swartz, E. R. Rosenberg, L. Beran, C. O. Avci, Y. Hikita, C. A. Ross, and H. Y. Hwang, Ferromagnetic resonance of perpendicularly magnetized $\text{Tm}_3\text{Fe}_5\text{O}_{12}/\text{Pt}$ heterostructures, *Appl. Phys. Lett.* **115**, 172402 (2019).
- [47] Y. V. Khivintsev, V. K. Sakharov, A. V. Kozhevnikov, G. M. Dudko, Y. A. Filimonov, and A. Khitun, Spin waves in YIG based magnonic networks: Design and technological aspects, *J. Magn. Magn. Mater.* **545**, 168754 (2022).
- [48] E. R. Rosenberg, K. Litzius, J. M. Shaw, G. A. Riley, G. S. D. Beach, H. T. Nembach, and C. A. Ross, Magnetic properties and growth-induced anisotropy in yttrium thulium iron garnet thin films, *Adv. Electron. Mater.* **7**, 2100452 (2021).
- [49] J. Zhang, W. Yu, X. Chen, and J. Xiao, A frequency-domain micromagnetic simulation module based on COMSOL Multiphysics, *AIP Adv.* **13**, 055108 (2023).
- [50] S. S. S. Kalarickal, P. Krivosik, M. Wu, C. E. E. Patton, M. L. L. Schneider, P. Kabos, T. J. J. Silva, and J. P. P. Nibarger, Ferromagnetic resonance linewidth in metallic thin films: comparison of measurement methods, *J. Appl. Phys.* **99**, 093909 (2006).
- [51] Y. Li, *et al.*, Reconfigurable spin current transmission and magnon-magnon coupling in hybrid ferrimagnetic insulators, *Nat. Commun.* **15**, 6 (2024).

- [52] Z. Zhang, H. Yang, Z. Wang, Y. Cao, and P. Yan, Strong coupling of quantized spin waves in ferromagnetic bilayers, *Phys. Rev. B* **103** (1), 104420 (2021).
- [53] F. Hoffmann, Dynamic pinning induced by nickel layers on permalloy films, *Physica Status Solidi (B)* **41**, 807 (1970).
- [54] X. Zhang, C. L. Zou, L. Jiang, and H. X. Tang, Strongly coupled magnons and cavity microwave photons, *Phys. Rev. Lett.* **113**, 1 (2014).
- [55] Behrouz Khodadadi, Anish Rai, Arjun Sapkota, Abhishek Srivastava, Bhuwan Nepal, Youngmin Lim, David A. Smith, Claudia Mewes, Sujan Budhathoki, Adam J. Hauser, Min Gao, Jie-Fang Li, Dwight D. Viehland, Zijian Jiang, Jean J. Heremans, Prasanna V. Balachandran, Tim Mewes, and Satoru Emori, Conductivitylike Gilbert damping due to intraband scattering in epitaxial iron, *Phys. Rev. Lett.* **124**, 157201 (2020).
- [56] Yi Li, Fanlong Zeng, Steven S.-L. Zhang, Hyeondeok Shin, Hilal Saglam, Vedat Karakas, Ozhan Ozatay, John E. Pearson, Olle G. Heinonen, Yizheng Wu, Axel Hoffmann, and Wei Zhang, Giant anisotropy of Gilbert damping in epitaxial CoFe films, *Phys. Rev. Lett.* **122**, 1 (2019).
- [57] Y. Xiong, Y. Li, M. Hammami, R. Bidthanapally, J. Sklenar, X. Zhang, H. Qu, G. Srinivasan, J. Pearson, A. Hoffmann, V. Novosad, and W. Zhang, Probing magnon–magnon coupling in exchange coupled $\text{Y}_3\text{Fe}_5\text{O}_{12}$ /permalloy bilayers with magneto-optical effects, *Sci. Rep.* **10**, 1 (2020).
- [58] B. Lenk, H. Ulrichs, F. Garbs, and M. Münzenberg, The building blocks of magnonics, *Phys. Rep.* **507**, 107 (2011).
- [59] P. Che, K. Baumgaertl, A. Kúkol'ová, C. Dubs, and D. Grundler, Efficient wavelength conversion of exchange magnons below 100 nm by magnetic coplanar waveguides, *Nat. Commun.* **11**, 1 (2020).